

The Southern Stellar Stream Spectroscopic Survey (S^5): Overview, Target Selection, Data Reduction, Validation, and Early Science

T. S. Li^{1,2,3,4}★, S. E. Koposov^{5,6}, D. B. Zucker^{7,8}, G. F. Lewis⁹, K. Kuehn^{10,11}, J. D. Simpson¹², A. P. Ji¹†, N. Shipp^{13,4,3}, Y.-Y. Mao^{14,15,16}‡, M. Geha¹⁷, A. B. Pace¹⁸, A. D. Mackey¹⁹, S. Allam³, D. L. Tucker³, G. S. Da Costa¹⁹, D. Erkal²⁰, J. D. Simon¹, J. R. Mould²¹, S. L. Martell^{12,22}, Z. Wan⁹, G. M. De Silva¹¹, K. Bechtol²³, E. Balbinot²⁴, V. Belokurov⁶, J. Bland-Hawthorn^{9,22}, A. R. Casey²⁵, L. Cullinane¹⁹, A. Drlica-Wagner^{3,13,4}, S. Sharma^{9,22}, A. K. Vivas²⁶, R. H. Wechsler^{27,28,29}, B. Yanny³

(S^5 Collaboration)

(Affiliations are listed after the references)

Accepted XXX. Received YYY; in original form ZZZ

ABSTRACT

We introduce the Southern Stellar Stream Spectroscopy Survey (S^5), an on-going program to map the kinematics and chemistry of stellar streams in the Southern Hemisphere. The initial focus of S^5 has been spectroscopic observations of recently identified streams within the footprint of the Dark Energy Survey (DES), with the eventual goal of surveying streams across the entire southern sky. Stellar streams are composed of material that has been tidally striped from dwarf galaxies and globular clusters and hence are excellent dynamical probes of the gravitational potential of the Milky Way, as well as providing a detailed snapshot of its accretion history. Observing with the 3.9-m Anglo-Australian Telescope’s 2-degree-Field fibre positioner and AAOmega spectrograph, and combining the precise photometry of DES DR1 with the superb proper motions from *Gaia* DR2, allows us to conduct an efficient spectroscopic survey to map these stellar streams. So far S^5 has mapped 9 DES streams and 3 streams outside of DES; the former are the first spectroscopic observations of these recently discovered streams. In addition to the stream survey, we use spare fibres to undertake a Milky Way halo survey and a low-redshift galaxy survey. This paper presents an overview of the S^5 program, describing the scientific motivation for the survey, target selection, observation strategy, data reduction and survey validation. Finally, we describe early science results on stellar streams and Milky Way halo stars drawn from the survey. Updates on S^5 , including future public data releases, can be found at <http://s5collab.github.io>.

Key words: Galaxy: halo - Galaxy: kinematics and dynamics - globular clusters: general - galaxies: dwarf

1 INTRODUCTION

Within the Λ CDM cosmological model, large galaxies grow hierarchically through the accretion of smaller systems. In the inner parts of galaxies, where dynamical time-scales are relatively short, these accreted systems are rapidly phase-mixed into a comparatively smooth stellar halo. However, in the outer stellar halo, where dynamical time-scales are longer, accreted systems are only partially phase

mixed, exhibiting the signatures of ongoing tidal disruption. Hence, the distribution of stellar debris in the halo provides a snapshot of the galactic evolution of our Milky Way (Freeman & Bland-Hawthorn 2002; Bullock & Johnston 2005).

The structural and kinematic properties of tidal stellar streams also provide a measurement of the mass and shape of the Milky Way’s dark matter halo. While this dark matter dominates the gravitational potential of the Milky Way, there remain significant uncertainties in its properties, limiting the accuracy of comparisons to predictions of hierarchical structure formation models. Hence, modelling the dynamical properties of a large sample of stellar streams, spread over a broad range of Galactocentric distances, offers the

★ Email: tingli@carnegiescience.edu; NHFP Einstein Fellow

† Hubble Fellow

‡ NHFP Einstein Fellow

realistic prospects of accurately determining Galaxy’s gravitational potential (e.g. Johnston et al. 1999; Bonaca & Hogg 2018).

Over recent years, there have been significant efforts to uncover stellar substructure in our Galactic halo, with more than fifty stellar streams now known, half of which were discovered in the last three years (Mateu et al. 2018, and references therein). In particular, the Dark Energy Survey (DES), with its unprecedented photometric calibration, depth, and sky coverage, has recently recovered four previously known stellar streams (Koposov et al. 2014; Drlica-Wagner et al. 2015; Balbinot et al. 2016; Grillmair 2017) and discovered eleven new streams in the Southern sky through isochrone matching of metal-poor populations throughout the stellar halo (Shipp et al. 2018). While imaging surveys, such as DES, can provide on-sky locations and distance estimates through isochrone fitting, spectroscopy is essential for measuring the kinematic and chemical properties of stream stars, allowing the determination of radial velocities, velocity dispersions, and gradients; this information is required to deduce the dynamical history of a stellar stream and infer the three-dimensional structure of the Milky Way’s dark matter halo (e.g. Ibata & Lewis 1998; Ibata et al. 2001; Koposov et al. 2010; Varghese et al. 2011; Gibbons et al. 2014; Bowden et al. 2015; Erkal et al. 2016; Bovy et al. 2016; Bonaca & Hogg 2018; Erkal et al. 2019). Spectroscopy is also crucial when using streams to measure the properties of dark matter subhaloes (e.g. Ibata et al. 2002; Johnston et al. 2002) since subhalo impacts create correlated signals in all of the stream observables (e.g. Yoon et al. 2011; Carlberg 2013; Erkal & Belokurov 2015a; Helmi & Koppelman 2016; Sanders et al. 2016; Bovy et al. 2017) and at least three observables are needed to recover the subhalo properties (Erkal & Belokurov 2015b).

Spectroscopy of stellar streams is challenging due to the relative faintness of stream-member stars ($g \sim 19$, for a horizontal branch star at 45 kpc), the low stellar surface density, with only several stars per deg^2 at $g \sim 19$, and substantial contamination from Milky Way foreground stars, with hundreds per deg^2 at $g \sim 19$. Despite the rapid increase in the number of known streams, these observational challenges have limited their detailed spectroscopic investigation, and hence their use as cosmological probes (see e.g., Majewski et al. 2004; Koposov et al. 2010; Sesar et al. 2015; Ibata et al. 2016). In order to investigate accretion processes and progenitors, we place a premium on assembling a large sample of streams, a large sample of stars per stream, and accurate kinematics, in the expectation that stream kinematics, including internal kinematics, retain a memory of initial conditions.

The Southern Stellar Stream Spectroscopic Survey (S^5) was initiated in mid-2018 to address the challenges associated with spectroscopic observations of stellar streams. To date, S^5 represents the first spectroscopic survey of stellar streams in our Galactic halo. S^5 uses the Two-degree Field (2dF) fibre positioner (Lewis et al. 2002) coupled with the dual-arm AAOmega spectrograph (Sharp et al. 2006) on the 3.9-m Anglo-Australian Telescope (AAT); 2dF provides 392 science fibres that can be distributed across a field of view (FOV) of $\sim 3 \text{ deg}^2$. S^5 is an ongoing survey, with 25 nights observed in 2018 and 12 hrs observed in 2019 as of June 2019, and more nights planned in 2019. Though S^5 intends to expand the targeted streams to the entire Southern Sky, our 2018 observations primarily targeted streams in the DES footprint. Therefore, this paper will mainly focus on the target selection and observations of the 14 DES streams.¹

¹ There are 15 streams identified in the DES footprint (Shipp et al. 2018).

The target selection for S^5 uses the recently released parallax and proper motion information from *Gaia* DR2 (Prusti et al. 2016; Gaia Collaboration et al. 2018a), together with precise photometry from the latest data releases of ground-based imaging surveys, mainly DES DR1 (DES Collaboration et al. 2018). Although 2dF provides substantial spectroscopic multiplexing, the diffuse nature of stellar streams still requires efficient target selection. Fortunately, proper motions from *Gaia* DR2 have dramatically improved the target selection efficiency of stream candidates, which allows us to conduct two auxiliary science programs with spare fibres: a Milky Way halo star survey and a low redshift (low- z) galaxy survey. While S^5 is mainly focused on stellar streams, this paper also provides an overview of the experimental design, target selection and data reduction of, and some early science from those auxiliary surveys.

The structure of this paper is as follows: Section 2 presents the details of the field and target selection for S^5 , while Section 3 details the observational program and subsequent data reduction. Section 4 lays out the validation of the survey, followed by a discussion of early science results in Section 5. Our conclusions and plans for the future of S^5 are presented in Section 6.

We note that in this paper, we use lower case *griz* for DECam photometry (except for Section 2.3.4 on SkyMapper photometry), where the photometry comes from either DES DR1 or the Dark Energy Camera Legacy Survey (DECaLS) DR7 (Dey et al. 2019), and we use G, G_{BP}, G_{RP} for *Gaia* photometry. We use the subscript 0 to denote the reddening-corrected photometry throughout the paper. For DECam photometry, the reddening correction was performed following the procedures described in DES DR1. Specifically, we calculated the extinction by multiplying the colour excess $E(B - V)$ from Schlegel et al. (1998) with the extinction coefficients taken from DES DR1 (DES Collaboration et al. 2018). For the *Gaia* photometry, we use the colour-dependent extinction corrections from Gaia Collaboration et al. (2018b) and the Schlegel et al. (1998) values of $E(B - V)$.

2 SURVEY DESIGN AND TARGET SELECTION

In this section, we first define the AAT fields for S^5 (Section 2.1), and then we discuss the target selection for each field, including stream targets, halo targets and the low- z targets. The 2dF fibre allocation software CONFIGURE² (Miszalski et al. 2006) allows the targets to be given a priority in the range 1–9 (P1–P9, with P9 being the highest). The higher the target priority, the more likely it is to be allocated a fibre by CONFIGURE. We therefore assigned our stream targets to the highest priority range (P9–P7), halo targets to the next priority range (P6–P3), and the low- z galaxy targets to the lowest priorities (P2–P1). In Table 1, we summarise the targets for each priority category. We detail the stream targets in Section 2.2, non-stream stellar targets in Section 2.3, and galaxy targets in Section 2.4. Some targets could fall in multiple priority categories; in those cases the highest priority was assigned.

2.1 Field Selection

In defining the AAT fields for S^5 , and considering the FOV of 2dF, the goal of our survey design is to cover the maximum sky

The Palca stream is not considered in S^5 due to its low surface brightness and diffuse morphology.

² <https://www.aao.gov.au/science/software/configure>

Table 1. Description of P9 to P1 targets for *S*⁵.

Priority	Target Description
P9	Stream candidates: metal-poor, PM1 (tight PM cut)
P8	Stream candidates: PM2 (less tight PM cut)
P7	Stream candidates: metal-poor, PM3 (loose PM cut)
P6	Rare objects (BHBs, RRLs, WDs)
P5	Extreme metal-poor star candidates (SkyMapper photometry)
P4	Metal-poor stars (DES photometry)
P3	Low PM stars
P2	High-probability low-z galaxy candidates
P1	Low-probability low-z galaxy candidates

area within the limited amount of total telescope time available. In summary, we separate AAT pointings by 2°, just under the diameter of the 2dF FOV, aligned with each stream’s ridgeline. For most streams, the ridgeline is defined as the heliocentric great circle from the end points of the stream defined in Shipp et al. (2018). For these streams, we make the field grid in the stream coordinates along stream latitude $\phi_2 = 0^\circ$ and stream longitude $\phi_1 = \dots, -2^\circ, 0^\circ, 2^\circ, \dots$, and then we transfer from stream coordinates to celestial coordinates using the rotation matrix for each stream.³ The only exception is the ATLAS stream, for which Shipp et al. (2018) found that the stream ridgeline deviates significantly from a great circle. We therefore used the polynomial track defined in Shipp et al. (2018) as the ridgeline for the ATLAS stream in our field definition.

The number of fields used for each stream depends on the length of the stream. For most streams, we have $L/2$ (rounded to the nearest integer) AAT fields, where L is the length of the stream in degrees from Shipp et al. (2018). For some streams, we obtained 1–2 extra AAT fields extending from the endpoints of the streams, to search for possible members beyond the photometric extent.

An illustration of the stream fields is shown in Figure 1 and the centres of the fields are listed in Table 2. Among the 14 DES streams, 10 streams have more than 80% of their observations completed to date: Tucana III, ATLAS, Aliqa Uma, Chenab, Elqui, Jhelum, Indus, Phoenix, Ravi, and Willka Yaku. The other four streams are planned for observation in 2019.

Before the start of *S*⁵, we carried out pilot programs on some of the stream fields, shown as the red filled circles in Figure 1. The Tucana III stream (at $\alpha_{2000} \sim 0^\circ$ and $\delta_{2000} \sim -60^\circ$) was observed in 2016 and was published in Li et al. (2018b). Two fields in the ATLAS stream were observed in 2018A. Proper motions from *Gaia* were not available then and therefore the target selection strategy described below does not apply to those pre-*S*⁵ fields. However, data collected from these two ATLAS fields are still considered as part of *S*⁵ in the data reduction and final catalogue production since the instrument settings were the same.

In addition, a few streams outside of the DES footprint were observed. The field selection presented here, as well as the target selection strategy described below, do not apply to those non-DES fields and we discuss them in Section 2.6.

³ The rotation matrices are defined in the Appendix C of Shipp et al. (submitted).

2.2 Stream Targets (P9–P7)

We first cross-match DES DR1 with *Gaia* DR2 by selecting a DES DR1 nearest neighbour for each *Gaia* source having separation $< 1''$. We do not use the proper motion information to account for possible high proper motion stars in the cross-match because the DES observations were conducted mostly while the *Gaia* mission was ongoing (i.e., they were observed at the same epoch). We then select our stellar targets from this joint catalogue as stream candidates.

From this joint catalogue, we first perform a stellar selection when the objects have

$$\text{WAVG_SPREAD_MODEL_I} < 0.005, \tag{1}$$

or

$$\text{ASTROMETRIC_EXCESS_NOISE} < 2, \tag{2}$$

where WAVG_SPREAD_MODEL_I is a weighted averaged (WAVG) SExtractor model-based star-galaxy separation quantity (Morganson et al. 2018) in *i*-band from DES DR1. The ASTROMETRIC_EXCESS_NOISE is the measure of the scatter of astrometric measurements around the solution from *Gaia* DR2 above what is expected from a noise model (Lindgren et al. 2016, 2018). This statistic identifies sources with bad astrometry and/or extended sources (e.g., galaxies) (Koposov et al. 2017). We note that this is a very conservative selection because we do not want to miss any possible stellar targets. In addition, we reject stars with parallax measurements consistent with being local disk stars. Specifically, we perform a parallax cut of

$$\text{PARALLAX} - 3 \times \text{PARALLAX_ERROR} < 0.2, \tag{3}$$

to remove stars with significant parallax measurements.

The bright-end magnitude limit is at $r_0 \sim 15$, which is close to the saturation limit of DES DR1.⁴ The faint end magnitude limit is generally at $r_0 \sim 19.5$, but varies slightly from stream to stream. For example, considering the distance of the Elqui stream ($\gtrsim 40$ kpc), we set the faint end limit at $r_0 = 19.8$. For closer streams, such as Jhelum and Indus, we set a brighter faint end at $r_0 = 19.0$.

We then further subdivide the candidate stars using (i) isochrone filtering in colour–magnitude space; (ii) metal-poor star selection in colour–colour space; and (iii) likely member selection in proper motion (PM) space. Figure 2 shows the selection process for one field in the ATLAS stream as an example. These selection criteria are as follows:

⁴ We note that stars at $r_0 \sim 15$ may suffer some saturation problems. However, we still include these targets, as bright stream members are rare.

Table 2. S^5 fields observed with the AAT as of June 2019. Columns from left to right are field name, RA and Decl. of the centre of the fields, UT date of the observation (with highest S/N if observed multiple times), MJD (start) of the observation, total exposure time (in seconds), average *Gaia* G -band magnitude at S/N = 5 per pixel (from red arm spectra), total number of targets (N_{targets}), and number of stars (N_{goodstar}) with good measurements (i.e. $\text{GOOD_STAR} = 1$; see definition in Section 4.5). We note that for fields in some streams such as ATLAS, Elqui, Phoenix, etc., N_{goodstar} is usually much lower than N_{targets} , because these streams are at high Galactic latitude; therefore, we used ~ 100 spare fibres to target low redshift galaxies (see Section 2.4), and all galaxy targets are assigned $\text{GOOD_STAR} = 0$ regardless of the quality of the spectra. All fields are grouped into four categories, which are fields in the DES footprint, fields outside the DES footprint (see Section 2.6), calibration fields for survey validation (see Section 4), and fields observed prior to S^5 with the same instrument setup but previously unpublished.

Field Name	RA (deg)	Decl. (deg)	UTDATE	MJD	t_{exp} (s)	$G@(S/N=5)$	N_{targets}	N_{goodstar}
ATLAS-0	30.350248	-33.098693	2018-09-14	58375.59	7200	18.9	347	182
ATLAS-1	28.406544	-31.922932	2018-09-13	58374.60	7200	19.1	359	188
ATLAS-3	24.569248	-29.628485	2018-09-12	58373.62	7200	18.8	359	187
ATLAS-4	22.671638	-28.507177	2018-09-27	58388.69	7200	18.6	359	140
ATLAS-5	20.784285	-27.396658	2018-10-26	58417.68	5800	18.4	345	153
ATLAS-6	18.912949	-26.299787	2018-09-11	58372.59	7200	18.7	359	185
ATLAS-7	17.046881	-25.215898	2018-10-23	58414.54	7200	18.4	359	162
ATLAS-8	15.186390	-24.141606	2018-10-26	58417.59	7200	18.5	359	156
ATLAS-10	11.485245	-22.025185	2018-09-08	58369.59	7200	18.7	359	185
ATLAS-11	9.638663	-20.985328	2018-09-27	58388.60	7200	18.5	348	165
Aliqa-Uma-1	39.653899	-37.658852	2018-09-08	58369.69	7800	18.7	347	222
Aliqa-Uma-2	37.776994	-36.334496	2018-09-07	58368.70	7600	18.8	347	215
Aliqa-Uma-3	35.965770	-34.980462	2018-09-09	58370.67	9600	19.0	347	219
Aliqa-Uma-4	34.211411	-33.603704	2018-08-09	58339.73	7200	19.1	348	211
Aliqa-Uma-5	32.515170	-32.198125	2018-08-08	58338.75	5400	18.8	308	191
Chenab-1	331.107304	-44.179689	2018-08-10	58340.46	7200	19.0	359	340
Chenab-2	330.109770	-46.053830	2018-08-10	58340.55	6700	18.6	348	288
Chenab-3	329.045873	-47.914236	2018-09-07	58368.41	7200	18.5	357	311
Chenab-4	327.900452	-49.766183	2018-09-11	58372.40	7200	18.9	359	328
Chenab-5	326.663567	-51.606374	2018-09-09	58370.39	7200	18.7	359	345
Chenab-6	325.321207	-53.432514	2018-09-08	58369.40	7200	18.6	359	341
Chenab-7	323.861828	-55.242360	2018-09-13	58374.42	7200	19.1	359	333
Chenab-8	322.259995	-57.036550	2018-08-09	58339.55	6300	19.0	348	324
Chenab-9	320.500812	-58.803070	2018-08-09	58339.46	6000	18.8	359	315
Elqui-0	22.107923	-43.089436	2018-09-14	58375.68	7800	18.7	359	187
Elqui-1	19.813988	-42.021790	2018-09-10	58371.59	9000	19.0	359	235
Elqui-2	17.594839	-40.909998	2018-08-09	58339.63	7800	19.0	348	166
Elqui-3	15.453303	-39.757473	2018-08-08	58338.66	7200	18.9	348	177
Elqui-4	13.383956	-38.560740	2018-09-09	58370.55	9000	18.8	359	187
Elqui-5	11.380964	-37.334282	2018-08-07	58337.59	7500	18.9	333	189
Indus-1	349.678452	-64.192996	2018-08-11	58341.66	3970	17.6	347	193
Indus-2	345.944962	-63.071643	2018-08-02	58332.73	7200	18.1	358	240
Indus-3	342.498793	-61.863658	2018-08-02	58332.66	5400	18.5	348	299
Indus-4	339.324859	-60.573093	2018-08-12	58342.61	5720	18.3	344	307
Indus-5	336.397623	-59.212635	2018-08-11	58341.55	7760	18.1	359	297
Indus-6	333.700573	-57.792776	2018-08-04	58334.74	6300	18.3	359	305
Indus-7	331.210566	-56.320239	2018-08-02	58332.59	5400	18.5	359	308
Indus-8	328.910308	-54.804194	2018-08-02	58332.52	5400	18.5	348	323
Jhelum-1	3.341637	-51.908154	2018-09-12	58373.53	7200	18.4	347	275
Jhelum-2	0.100185	-51.978971	2018-09-09	58370.48	5400	18.5	347	280
Jhelum-3	356.853568	-51.960940	2018-09-10	58371.49	7200	18.5	347	285
Jhelum-4	353.614405	-51.853841	2018-10-23	58414.44	7200	18.2	349	294
Jhelum-5	350.398170	-51.660569	2018-08-04	58334.67	6000	18.6	348	292
Jhelum-6	347.216054	-51.376758	2018-08-04	58334.60	5400	18.6	359	298
Jhelum-7	344.078713	-51.011100	2018-08-01	58331.64	7200	18.8	348	295
Jhelum-8	340.996359	-50.560674	2018-09-13	58374.51	6600	18.4	347	321
Jhelum-9	337.979644	-50.031113	2018-09-10	58371.40	7200	18.7	359	351
Jhelum-10	335.027230	-49.426959	2018-09-08	58369.50	7200	18.7	347	340
Jhelum-11	332.150927	-48.748199	2018-10-25	58416.54	5400	17.8	349	258
Jhelum-13	326.650541	-47.188388	2018-08-08	58338.60	4800	18.1	359	340
Jhelum-14	324.025939	-46.315883	2018-08-01	58331.51	7200	18.8	367	340
Phoenix-1	27.522755	-43.434219	2018-09-10	58371.70	7800	18.7	347	199
Phoenix-2	26.574314	-45.316320	2018-08-01	58331.73	7200	18.8	359	179
Phoenix-3	25.563754	-47.189449	2018-09-07	58368.60	7800	18.6	359	214
Phoenix-4	24.478430	-49.055840	2018-08-06	58336.61	9600	18.7	348	204
Phoenix-5	23.306432	-50.906988	2018-08-07	58337.76	5100	18.7	359	186
Phoenix-6	22.038990	-52.749837	2018-08-07	58337.69	5700	18.7	348	249
Phoenix-7	20.661395	-54.573383	2018-08-06	58336.70	7200	18.6	359	254
Ravi-0	344.584255	-60.354707	2018-10-26	58417.50	6900	18.3	349	302
Ravi-1	343.013169	-58.523030	2018-09-07	58368.51	7200	18.4	347	282
Ravi-2	341.596599	-56.670068	2018-09-14	58375.50	7200	18.7	359	324
Ravi-3	340.313034	-54.807171	2018-09-11	58372.49	7200	18.5	347	317
Ravi-4	339.142485	-52.930510	2018-09-29	58390.52	7200	18.4	359	320
Ravi-7	336.166823	-47.240314	2018-09-27	58388.50	7200	18.5	359	326
Ravi-8	335.318605	-45.326721	2018-09-12	58373.43	7200	18.6	359	321
Turraburra-8	60.602100	-18.782405	2018-10-24	58415.67	7200	18.4	349	269
Willka-Yaku-0	38.631197	-57.506521	2018-09-16	58377.70	7600	18.6	347	239
Willka-Yaku-1	38.037160	-59.482054	2018-09-11	58372.68	9600	18.7	347	223
Willka-Yaku-2	37.367524	-61.453825	2018-09-12	58373.71	7200	18.7	347	234
Willka-Yaku-3	36.606647	-63.423661	2018-09-13	58374.69	8100	18.8	347	285

Table 2 – continued

Field Name	RA	Decl	UTDATE	MJD	t_{exp}	$r(S/N=5)$	N_{targets}	N_{goodstar}
Orphan-0	333.495287	-35.792559	2018-09-16	58377.63	5400	18.0	96	67
Orphan-5	311.994544	-65.291570	2018-09-14	58375.46	3000	17.8	347	316
Orphan-6	300.961865	-70.170982	2018-10-24	58415.49	5400	17.3	347	318
Orphan-7	284.073327	-73.980884	2018-10-24	58415.42	5400	17.5	336	324
Orphan-8	260.292330	-75.842149	2018-09-14	58375.41	3000	17.9	359	336
Orphan-9	234.767419	-75.015676	2018-09-16	58377.46	3600	17.6	348	336
Orphan-10	214.945014	-71.858611	2018-09-16	58377.41	2700	17.5	359	337
Orphan-11	201.728540	-67.327261	2018-09-14	58375.37	2400	18.1	347	316
Orphan-13	246.613855	-75.778180	2018-09-29	58390.40	4500	17.8	359	336
Orphan-14	272.560733	-75.241258	2018-09-27	58388.44	4500	18.3	349	332
Orphan-15	293.352126	-72.317383	2018-09-29	58390.46	4500	18.1	349	336
Orphan-16	306.916290	-67.777798	2018-10-25	58416.47	5400	17.9	359	333
Orphan-17	316.524807	-62.124740	2018-10-26	58417.42	5400	18.1	355	318
Orphan-23	188.420550	-58.979594	2019-04-04	58577.64	3600	18.2	354	330
Orphan-24	184.921533	-55.456617	2019-04-01	58574.65	2700	17.4	354	344
Orphan-25	182.010398	-51.845786	2019-04-05	58578.65	2700	17.2	352	346
Orphan-26	179.579995	-48.163979	2019-04-03	58576.65	2700	17.2	354	329
Orphan-28	175.866616	-40.612588	2019-04-02	58575.64	3600	17.7	354	297
Orphan-30	173.301936	-32.863553	2019-04-04	58577.59	3600	18.0	342	318
Orphan-32	170.967451	-25.124912	2019-04-02	58575.59	3600	18.0	343	304
Orphan-33	169.618942	-21.320312	2019-04-06	58579.65	3060	17.5	354	249
Orphan-34	168.164652	-17.552359	2019-04-03	58576.59	4500	18.3	313	266
Orphan-35	166.635130	-13.805600	2019-04-06	58579.61	3300	18.3	350	269
Orphan-36	165.068830	-10.070858	2019-04-05	58578.59	4500	18.5	312	246
Orphan-38	161.936058	-2.604385	2019-04-01	58574.58	4500	18.4	298	211
Pal5-1	224.228739	-5.306396	2018-08-02	58332.37	5400	18.9	348	325
Pal5-2	225.553103	-3.721754	2018-08-02	58332.43	5400	18.7	359	288
Pal5-5	237.497969	4.857110	2018-08-10	58340.36	7200	19.1	348	331
Pal5-6	240.053281	5.941191	2018-08-09	58339.37	7200	18.9	348	328
Sgr-m1	295.703295	-34.788933	2018-08-12	58342.36	3600	17.6	344	342
Sgr-m2	286.648265	-32.139498	2018-09-10	58371.37	1200	15.9	347	345
Sgr-m3	300.428337	-35.849861	2018-10-26	58417.40	1800	17.6	315	309
Sgr-s1	297.638039	-29.602086	2018-08-12	58342.41	4200	17.7	359	338
Sgr-s2	288.958424	-27.174620	2018-09-12	58373.39	2600	17.7	347	342
Sgr-s3	301.946385	-31.119809	2018-09-13	58374.37	3000	18.1	318	310
calib-NGC6316	259.155679	-28.139205	2018-09-08	58369.37	1800	16.0	269	268
calib-NGC7078	322.492990	12.167678	2018-09-11	58372.38	1200	15.3	347	346
calib-NGC7089	323.364115	-0.823334	2018-09-16	58377.39	600	14.7	232	232
calib-Sgr1	283.900504	-30.799532	2018-09-09	58370.36	600	16.4	347	347
calib-Sgr4	281.600246	-30.100294	2018-09-07	58368.37	1800	15.1	347	347
atlas-test1	26.200215	-30.599785	2018-01-23	58141.43	7200	18.5	360	284
atlas-test2	13.305955	-23.062726	2018-06-06	58275.76	4500	18.6	360	260
Pal5-pt1	222.891667	-6.885655	2018-06-05	58274.58	7200	19.0	346	323
Pal5-pt2	222.959421	-11.185382	2018-06-06	58275.36	7200	19.3	349	327
Jhelum-pt1	341.012565	-50.501704	2018-06-06	58275.69	4800	17.9	349	344

(i) *Colour–magnitude space (Figure 2, upper-right panel)*: Considering the relatively metal-poor nature of known streams, we select targets in a window of either $|\Delta(g-r)| < 0.10$ or $|\Delta g| < 0.5$ from either a metal-poor ($[Fe/H] = -2.2$) or a relatively metal-rich ($[Fe/H] = -1.4$) Dartmouth isochrone (Dotter et al. 2008) for red giant branch (RGB) and main sequence turnoff (MSTO) candidates. The same criteria are applied to select blue horizontal branch (BHB) candidates using a M92 BHB ridgeline from Belokurov et al. (2007), built based on SDSS photometry from Clem (2006), and we transform from the SDSS photometry to the DES photometric system using equation (5) from Bechtol et al. (2015). For some streams, when the target density is low, we also increase the bandwidth of the selection. We note that we purposely discard the red horizontal branch (RHB) candidates, given that the RHB has large contamination from the foreground MSTO stars, which would result in a lower member identification efficiency.

(ii) *Colour–colour space (Figure 2, lower-left panel)*: As shown in Li et al. (2018b) and Pace & Li (2019), the location of stars in a dereddened $g-r$ vs $r-i$ diagram is correlated with the metallicity of the star (discussed in Section 5.3). Specifically, stars located above and to the left of the stellar locus (black solid line) tend to be more

metal poor than those below and to the right of the locus. Therefore, we select targets in a band between the stellar locus and a locus shifted $+0.06$ mag in $r-i$ (the black dashed line) as the metal-poor targets.

(iii) *Proper motion space (Figure 2, lower-right panel)*: Gaia DR2 proper motions greatly improve our target selection efficiency. The proper motion of each DES stream is measured in Shipp et al. (submitted). S^5 target selection used a preliminary version of these proper motions. For a given stream, three PM categories are selected:

- PM1: a tight PM selection with $|\mu_{\phi_i} - \mu_{\phi_{i,0}}| < 1 \text{ mas yr}^{-1}$;
- PM2: a less tight PM selection with $|\mu_{\phi_i} - \mu_{\phi_{i,0}}| < 2 \sim 3 \text{ mas yr}^{-1}$ (varying from stream to stream);
- PM3: a loose PM selection with $|\mu_{\phi_1}| < 4 \sim 5 \text{ mas yr}^{-1}$ and $|\mu_{\phi_2}| < 2 \sim 3 \text{ mas yr}^{-1}$ (varying from stream to stream);

where $i = 1$ or 2 and $\mu_{\phi_{1,0}}$ and $\mu_{\phi_{2,0}}$ are the PM of the stream and μ_{ϕ_1} and μ_{ϕ_2} are the PM in stream coordinates of the target star after solar reflex motion correction (assuming all the targets are at the distance of the stream from isochrone fitting).

We then assign stream targets to priority levels P9, P8, and P7,

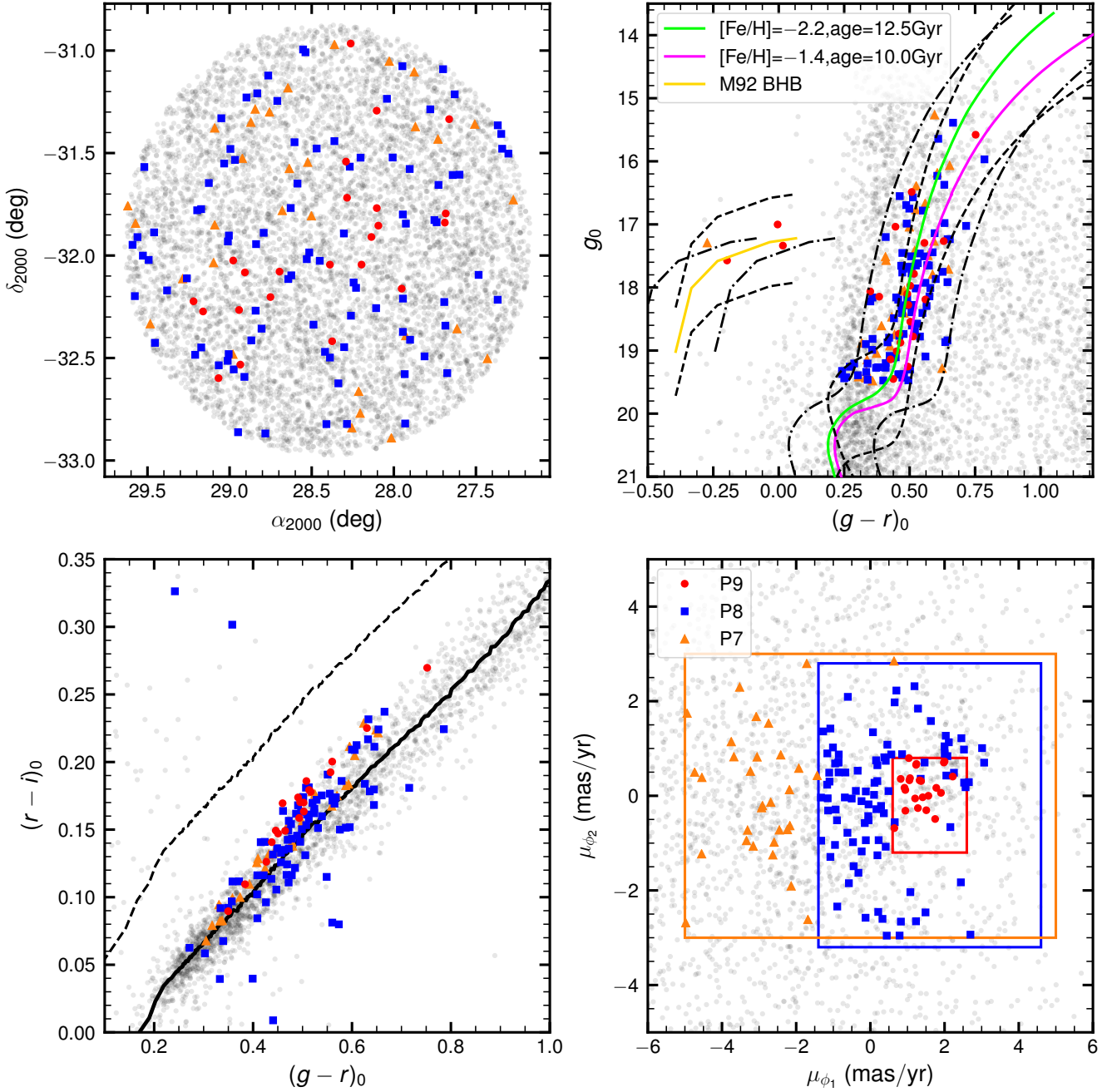


Figure 2. Illustration of the stream target selection in one AAT field. For all panels, grey dots represents all stars in DES DR1 \times Gaia DR2 in this field. P9, P8, P7 targets are shown in red circles, blue squares and orange triangles, respectively. *Upper-left:* Spatial distribution on the sky of the stream targets in one AAT field. *Upper-right:* Stream targets selected in colour–magnitude space. A more metal-rich ($[\text{Fe}/\text{H}] = -1.4$, lime curve) and a metal-poor ($[\text{Fe}/\text{H}] = -2.2$, magenta curve) Dartmouth isochrone are used to guide the selection for giant and MSTO candidates. The M92 BHB ridgeline is used to guide the selection for BHB candidates. Both black dashed and dot-dashed lines show the bandwidth of the selection. *Lower-left:* Stream candidates in colour–colour space. The black solid line is the stellar locus in DES $(g-r)_0$ vs $(r-i)_0$, and the dashed line is the stellar locus shifted by $+0.06$ mag in $(r-i)_0$. We select targets between these two lines as candidate metal-poor stars for the stream targets and used for P9 and P7 targets. *Lower-right:* Stream targets in proper motion space in stream coordinates (ϕ_1, ϕ_2) . Proper motions shown here are all corrected for the Sun’s reflex motion assuming stars are at the distance of the stream. Stream targets are selected to be centred on the proper motion of the stream measured in Shipp et al. (*submitted*), with a tight PM cut for P9 targets (red box), a less tight PM cut for P8 targets (blue box), and a loose PM cut (orange box, independent of the detected stream PM) for P7 targets.

2.3.1 P6: Blue Stars

Since blue stars are generally rare and bright, we set P6 for blue stars with $-0.4 < (g-r)_0 < 0.1$ and $15 < g_0 \lesssim 19.5$, where the faint end limit varies from stream to stream. Most stars in this selection are either blue horizontal branch stars (BHBs) or blue stragglers (BSs). The selection results in, on average, about 20-50 blue stellar targets within an AAT field, although it turns out that about one-third of these blue stellar targets are actually QSOs (see Section 4.4).

2.3.2 P6: RR Lyrae stars

RR Lyrae candidate stars are selected from two separate source catalogues, table `vari_classifier_result` and table `vari_rrlyrae`, released as part of the *Gaia* DR2 (see Clementini et al. 2019; Holl et al. 2018). The astrometry and photometry information are acquired by joining with the main `gaia_source` catalogue. We then selected the RR Lyrae targets with $15 < G < 20$. This results in several (1-5) stars on average per AAT field.

2.3.3 P6: White Dwarfs

We also include hot white dwarf candidates (WDs) in the P6 category. We note that these WDs are not necessarily halo stars, but they are considered part of the halo survey due to their low target density. Our interest in including these hot WD candidates as targets is in their potential future use as faint spectrophotometric standard stars for large surveys and large instruments in the Southern Hemisphere (e.g., Narayan et al. 2019).

Candidate hot WDs were selected from *Gaia* DR2, based on criteria for identifying WDs from the *Gaia* DR2 photometry and astrometry as described in Gentile Fusillo et al. (2019). When we created our sample, their paper was still in preprint form and we did not have a copy of their catalogue of candidate WDs, so we applied their criteria (with minor variations) to regenerate their final catalogue in the *Gaia* DR2 data ourselves. We further trimmed our sample using the following prescription:

- Since we are primarily interested in hot WDs within the DES footprint, we matched our catalogue to the DES DR1 catalogue, removing entries that had no matches.
- We also used the T_{eff} values from Sloan Digital Sky Survey (SDSS; York et al. 2000) stars modelled by the SEGUE Stellar Parameter Pipeline (Lee et al. 2008) to identify a colour cut that would select only those candidate WDs with $T_{\text{eff}} \gtrsim 10,000$ K. We then applied that colour cut ($g-r \lesssim 0.0$) to the WD candidates remaining from our match with the DES catalogue.
- In order to not waste fibres on candidates that had a low probability of being actual WDs, we imposed cuts based on *Gaia* photometry and astrometry that would include only those candidates with a probability of being a white dwarf of $P_{\text{WD}} \gtrsim 0.80$ from Gentile Fusillo et al. (2019).
- To avoid unnecessary duplication, we also excluded any white dwarf candidate that already had a spectrum from SDSS.

A plot showing our candidate hot WD targets in the *Gaia* HR diagram can be found in Figure 3. There are 13,019 candidate hot WD candidates over the full DES footprint in our list of potential P6 targets, and typically a few (1-4) were observed in each AAT field.

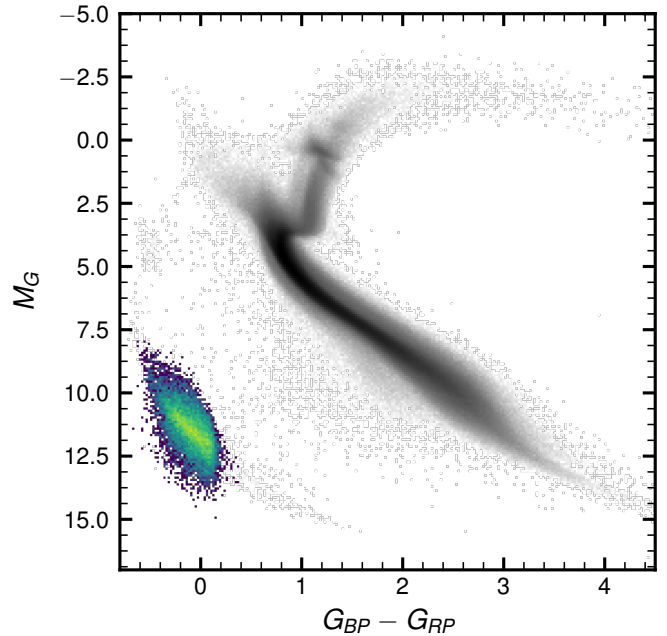


Figure 3. *Gaia* HR diagram constructed with all *Gaia* stars at $\text{PARALLAX}/\text{PARALLAX_ERROR} > 10$ and $E(B-V) < 0.02$. Also plotted as a 2D histogram is our targeted hot white dwarf candidate sample in the lower left corner, with yellow indicating higher density in each bin.

2.3.4 P5: Extremely Metal-Poor Candidates

We target, with priority P5, candidate stars selected as part of the SkyMapper search for extremely metal-poor (EMP) stars. As described by Da Costa et al. (submitted), these stars are selected using *vgi* photometry from Data Release 1.1 of the SkyMapper Southern Survey (Wolf et al. 2018). While the SkyMapper EMP program usually imposes a faint limit of $g \approx 16$, we relax this to $g = 17.5$ to boost the number of candidates per 2dF field to typically in the range $\sim 5 - 10$. Unsurprisingly, duplicate entries in the SkyMapper EMP list and the DES metal-poor halo star list (Section 2.3.5) sometimes occur; since the SkyMapper targets have P5 while the DES targets have P4, objects are preferentially allocated from the SkyMapper list.

2.3.5 P4: Metal-Poor Stars

P4 targets are selected to be metal-poor candidates using the dereddened $g-r$ vs $r-i$ colour of the stars, in a similar way as metal-poor star selection for streams described in Section 2.2 and in the lower left panel of Figure 2. To further minimise the target density, we select metal-poor targets that lie between 0.02 and 0.06 mag in $r-i$ above the empirical stellar locus, and $0.4 < (g-r)_0 < 1.0$, $15 < g_0 < 18.5$. This selection results in an additional $\sim 10 - 50$ targets per AAT field. For stream fields at low Galactic latitude ($|b| \lesssim 50^\circ$), P4 targets are not selected.

2.3.6 P3: Low Proper Motion Stars

P3 targets are selected to be stars with small proper motion and therefore are more likely to be distant halo stars. To make this selection, we first compute a reflex motion corrected proper motion for each star, based on their position on the sky, assuming that they

are all at 30 kpc from the Sun. We then select the targets with $|\mu_\alpha| < 3 \text{ mas yr}^{-1}$ and $|\mu_\delta| < 3 \text{ mas yr}^{-1}$ and $15 < g_0 < 18.5$. This selection results in $\sim 10 - 50$ targets per AAT field (depending on the Galactic latitude of each field). For stream fields at lower Galactic latitudes ($|b| \lesssim 50^\circ$), P3 targets are not observed.

2.4 Low- z Galaxy Targets (P2–P1)

Observations of nearby dwarf galaxies ($z < 0.02$, $M_r > -16$) are critical for understanding the mapping between dark matter and galaxy formation (Geha et al. 2017). However, these galaxies are difficult to distinguish from the far more numerous background galaxy population via photometry alone. The goal of including low-redshift (low- z) galaxy targets in S^5 is to increase the number of spectroscopically confirmed low- z galaxies in order to better train photometric selection algorithms, and help build a statistical sample of very low- z galaxies.

The galaxy targets are selected using the DES DR1 catalogue and are limited to the DES stream fields. To build the galaxy target list, we first select the objects that satisfy all of the following conditions:

IMAFLAGS_ISO_R = 0,
 FLAGS_R < 4, and
 EXTENDED_COADD = 3,

where the first two criteria are to select clean objects and EXTENDED_COADD is defined as:

EXTENDED_COADD =
 (SPREAD_MODEL_R + 3 × SPREADERR_MODEL_R > 0.005)
 +(SPREAD_MODEL_R + SPREADERR_MODEL_R > 0.003)
 +(SPREAD_MODEL_R – SPREADERR_MODEL_R > 0.003),

to select high-confidence galaxies based on SExtractor model-based star-galaxy separation⁵.

We also limit the galaxy targets to the magnitude range of $18 < r_0 < 20$, and to the fields within the Galactic Cap ($|b| > 50^\circ$).

After the initial selection, we then use the low- z galaxy data from the SAGA Survey⁶ (Geha et al. 2017) and the method outlined in Mao et al. (*in prep.*) to develop a set of photometric cuts that preferentially select very low- z galaxy candidates. They are cuts in the colour–colour, colour–magnitude, and surface brightness–magnitude spaces:

$(g_0 - r_0) > (r_0 - i_0 - 0.05) \times 2$;
 $(g_0 - r_0) < 2 - (r_0/14)$;
 $SB_r > 0.9r_0 + 5.25$;

and are shown in Figure 4. Here, SB_r is the surface brightness derived from r -band magnitude and flux radius. We only select galaxies that pass all three photometric cuts. We then further prioritize these candidates into high (P2) and low (P1) priority using a multivariate Gaussian Mixture Model (GMM) trained in colour space ($grizY$) on both synthetic data and SAGA spectroscopic data. The GMM probabilities are also shown in the colour–colour panel of Figure 4 for reference.

While our photometric cuts preserve very high completeness for very low- z (up to $z < 0.02$) galaxies (Mao et al. *in prep.*), due

to incomplete sampling of these lower priority targets, the resulting sample cannot be considered complete. However, even an incomplete sample serves our goal of obtaining training data for photometric selection algorithms that are tuned to very low- z ranges.

2.5 Stream Overlaps

Some AAT fields targeting different streams have partial overlap. In these cases, we have only observed the fields defined for one of the streams, but we select stream candidates from both streams as targets. These fields include (see Figure 1 and Table 2) Chenab-3 (overlap w/ Jhelum), Chenab-5 (w/ Ravi), Chenab-6 (w/ Ravi), Jhelum-9 (w/ Indus), Jhelum-10 (w/ Indus). In these fields, P9 and P7 are the two categories for stream candidates in the primary stream, and P8 and P6 are the two categories for the stream candidates in the overlapping stream. No further targets from the halo or low- z surveys are considered in these fields.

2.6 Streams Beyond DES

While this paper focuses on the target selection and observations for the DES streams, we also observed some streams beyond the DES footprint, including the Orphan stream, the Sagittarius stream, and the Palomar 5 stream. Observations of these streams were taken while the DES streams were not observable for parts of the night. We used different input photometric catalogues, target selection and field selection criteria for each stream, to fulfill different science goals on each stream. For example, Orphan stream targets are selected to be the extensions of the Chenab stream using *Gaia* DR2 photometry and proper motion in order to map the entire Orphan Stream in the Southern Hemisphere. Sagittarius stream targets were selected to study the stream bifurcation using *Gaia* DR2 photometry and proper motion. Palomar 5 stream candidates were targeted using Pan-STARRS1 photometry (Chambers et al. 2016) and *Gaia* proper motions to search the extension beyond the known length of the stream. Since each stream was treated differently, we will leave a more detailed description of the data on these streams for future publications. We note, however, that the data collected for these streams were reduced and validated alongside the rest of the S^5 data, as discussed in Section 3 and 4.

We also note that in 2019, S^5 plans to extend the survey beyond the DES streams and map more streams at $\delta_{2000} < 30^\circ$.

3 OBSERVATIONS AND REDUCTION

3.1 Observations

As previously noted, S^5 used the AAOmega spectrograph on the 3.9-m Anglo-Australian Telescope, located at the Siding Spring Observatory in Australia. AAOmega is a dual arm spectrograph, with the light split by a dichroic centred at 5800 Å. The gratings employed were 580V on the blue arm, and 1700D on the red arm, corresponding to spectral resolutions of ~ 1300 and ~ 10000 . With these, the blue side wavelength coverage is 3800 – 5800 Å, while the coverage on the red side is 8420 – 8820 Å. The gratings were chosen so that we could have the highest spectral resolution in the red centred on the near-infrared calcium triplet (CaT) lines to derive precise radial velocities of stream members, and the largest spectral coverage in the blue for fainter stars as well as galaxies for spectroscopic redshift determination.

To obtain sufficient signal-to-noise (S/N) on our faintest targets,

⁵ <https://des.ncsa.illinois.edu/releases/dr1/dr1-faq#faq1>

⁶ <http://sagasurvey.org>

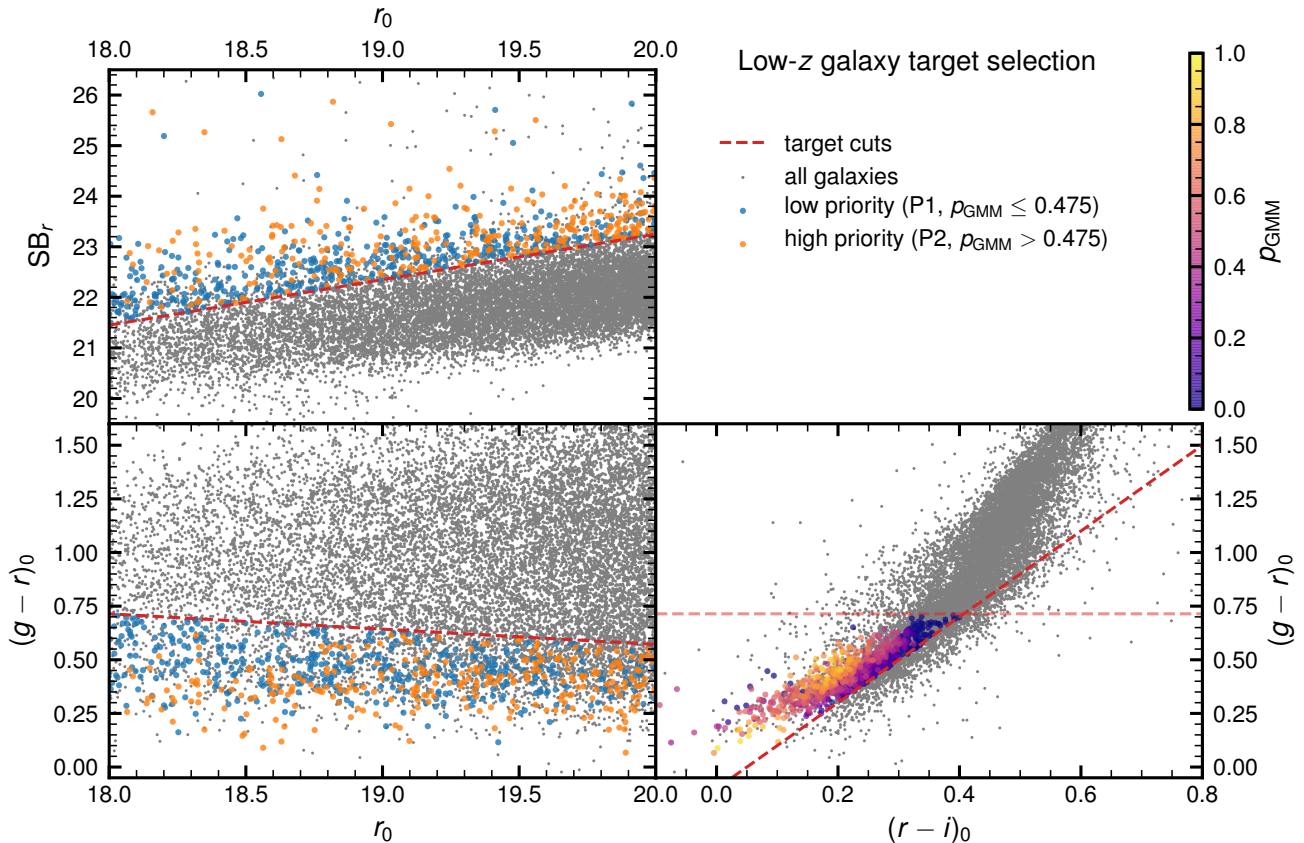


Figure 4. The three panels demonstrate our low- z galaxy target selection in the surface brightness–magnitude (*upper left*), colour–magnitude (*lower left*), and colour–colour (*lower-right*) spaces. The red dashed lines in each panel show the photometric cuts that preferentially select the very low- z galaxies (see Sec. 2.4 for cut definitions), and we select only galaxies that pass all three cuts to be our targets. We then use a multivariate Gaussian Mixture Model in the *grizY* space to assign a probability (p_{GMM}) to each of the galaxy candidates (as shown by the colour dots in the lower right panel), and assign candidates that have $p_{\text{GMM}} > 0.475$ to P2 (high-priority low- z targets, shown as orange dots in the left panels), and the rest to P1 (low-priority low- z targets, shown as blue dots in the left panels).

each DES stream field was observed with a total integration time of ~ 7200 seconds,⁷ split into three equal exposures to mitigate cosmic ray contamination. The average resulting S/N of stellar targets at $r \sim 18.5 - 19.0$ (see Table 2) is ~ 5 per pixel in the red arm (at a pixel scale of $\sim 0.23 \text{ \AA pixel}^{-1}$), allowing velocity determinations at a precision of $\sim 1 \text{ km s}^{-1}$. Furthermore, calibration exposures, consisting of arc spectra and a quartz fibre flat field, were obtained for each field right before or after the science exposures, while a series of bias exposures were obtained before the night’s observing began.

The observation date and exposure time for each field are listed in Table 2. We re-observed a few fields if the first observation on the field was obtained in unfavourable weather conditions; in such cases, Table 2 only includes the observations taken under the best conditions.

We had a total of 25 nights of observing time spread over 29 nights (with some half-nights) spanning from August 2018 to October 2018. We lost approximately 5 nights in total due to poor weather (either too cloudy or seeing $> 3''$). The remaining 20 nights had good weather, with an average seeing of $\sim 1''.5$. In April 2019, we obtained another ~ 12 hr of observations with good seeing

conditions of $\sim 1''.5$ or better, which we devoted entirely to the Orphan Stream because the DES streams were not visible. More observations are planned and will be executed later in 2019.

During our observations, we found that some fibres have lower-than-expected throughput, likely caused by the fibre placement accuracy. This can severely degrade the S/N for these fibres especially under good seeing conditions (seeing $< 1''$), and we discuss this issue in more detail in Appendix A.

3.2 Data Reduction

3.2.1 2DFDR reduction

The initial data reduction was undertaken with the 2DFDR software package (AAO Software Team 2015), which automatically performs the standard reduction steps for multi-fibre data: debiasing the CCD frames, tracing the location of the stellar spectra from the location of tramlines drawn from the fibre flat, then wavelength calibration, and extracting the 1D spectra.

The blue arm (580V grating) data were reduced using the OzDES (Yuan et al. 2015) reduction parameter files. The red arm (1700D grating) data were reduced using the default settings, except for the following changes: we chose a 2D fit for the scattered light subtraction, a 7th order polynomial fit for the fitting of the wave-

⁷ For non-DES streams, the integration time varies from stream to stream depending on the science goals.

length solution of the arcs, and a 1st order polynomial fit to the sky lines for additional wavelength calibration.

We note that one-quarter of the observations were taken at or near full-moon. For those observations, the extracted 1D spectra from the blue arm data show negative fluxes in the continuum or contamination by solar spectrum, which was likely caused by imperfect sky subtraction when the sky background is strong. Therefore, the blue arm spectra taken under full moon should be used with caution. For stellar targets, as discussed later in Section 4, we mostly used the measurements from the red arm spectra for future analysis. For galaxy targets, since only blue arm spectra were used for redshift determination (see Section 3.2.4), those spectra suffering strong sky background were discarded.

3.2.2 Fitting the spectra with *rvspecfit*

To determine the spectral atmospheric parameters and radial velocities (RVs) of each star, we have run each targeted spectrum through the template fitting code *rvspecfit*⁸ built for large stellar survey RV fitting. The code is loosely built on the template fitting described in [Koposov et al. \(2011\)](#). Given the stellar template $T(\lambda|\phi, v)$, stellar atmospheric parameters ϕ , radial velocity v , and observed spectra D_i with errors E_i observed at wavelengths λ_i at pixels i , the code performs a least-squares fit to the observed spectra using a spectral template multiplied by a polynomial continuum $T(\lambda|\phi, v)(\sum_j a_j \lambda^j)$. Thus *rvspecfit* provides the log-likelihood of the data given stellar atmospheric parameters after marginalizing over polynomial continuum coefficients. The stellar templates are determined by the following stellar atmospheric parameters ϕ : effective temperature T_{eff} , surface gravity $\log g$, metallicity $[\text{Fe}/\text{H}]$ and alpha elements abundance $[\alpha/\text{Fe}]$. For a given set of stellar atmospheric parameters, a stellar template is generated through a two-stage interpolation procedure. First we take the PHOENIX-2.0 high-resolution stellar spectra library ([Husser et al. 2013](#))⁹, which have been computed on a sparse grid of stellar atmospheric parameters. We note that the step-size of the grid is quite large ($\Delta \log g = 0.5$, $\Delta [\text{Fe}/\text{H}] = 0.5$ to 1). We truncate the spectra in the grid to the AAT wavelength range and convolve them to the appropriate resolution ($R \sim 1300$ for 580V and $R \sim 10000$ for 1700D). After that we use the Radial Basis Function (RBF) multiquadric interpolation over the grid to evaluate templates on a stellar atmospheric parameter grid with smaller and uniform steps in $[\text{Fe}/\text{H}]$ (0.25 dex) and $[\alpha/\text{Fe}]$ grid (0.2 dex), while preserving the uniform step of 0.5 dex in $\log g$ and non-uniform sampling of T_{eff} from the original grid. This creates a finer, more uniform grid and fills in some isolated gaps present in the original PHOENIX-2.0 grid. The multiquadric interpolation step is only performed once when preparing for fitting of the AAT instrument spectra. A final stage of stellar template generation is performed during each likelihood evaluation on each observed spectrum from 2DFDR. It is done by *rvspecfit* code using linear N-D interpolation between the templates based on the Delaunay triangulation (see e.g. [Amidror 2002](#)) as implemented in `SCIPY.INTERPOLATE.LINEARNDINTERPOLATE`. This interpolation is fast enough to be done in each likelihood evaluation and provides smoothly changing spectral templates as a function of stellar atmospheric parameters.

With the data likelihood function described above, we sample

the posterior of stellar atmospheric parameters and radial velocities of each star. To initialise the starting points of the Markov Chain, the fits are preceded by a cross-correlation step over a subset of templates, followed by a Nelder-Mead search of the maximum likelihood point in the space of stellar atmospheric parameters and RVs.

The priors adopted for the MCMC sampling are uniform over $\log g$, $[\text{Fe}/\text{H}]$, $[\alpha/\text{Fe}]$, and RV. The prior range for the stellar parameters are determined by PHOENIX-2.0 limits; for RV we set the range to be between $\pm 2000 \text{ km s}^{-1}$. The only informative prior used is on the effective temperature T_{eff} , for which the prior is based on the colours and metallicities of the stars. We have two separate T_{eff} prior models, $\pi(T_{\text{eff}}|\text{Gaia photometry})$ and $\pi(T_{\text{eff}}|\text{DECam photometry})$. The latter is used in the fitting when DECam photometry is available, from either DES or DECaLS ([Dey et al. 2019](#)), and the former is used when only Gaia photometry is available. Rather than trying to construct a conventional polynomial prior for T_{eff} based on colours and metallicity ([Alonso et al. 1999](#)), we fit a function $\log T_{\text{eff}}(\text{colours}, [\text{Fe}/\text{H}])$ using a gradient-boosted tree (see e.g. [Bishop 2006](#)) as implemented in `SKLEARN.ENSEMBLE`. We use the SDSS and SEGUE effective temperatures from SDSS DR9 ([Lee et al. 2008](#); [Allende Prieto et al. 2008](#)) and the $G_{BP} - G_{RP}$ Gaia colours and $g - r$, $r - z$ DECam colours to train the model.¹⁰

Specifically we fit three functions, $T_{\text{eff},50}(\text{colours}, [\text{Fe}/\text{H}])$, $T_{\text{eff},16}(\text{colours}, [\text{Fe}/\text{H}])$, $T_{\text{eff},84}(\text{colours}, [\text{Fe}/\text{H}])$, using quantile regression corresponding to the 16%, 50%, 84% percentiles of the $T_{\text{eff}}|\text{colours}, [\text{Fe}/\text{H}]$ distribution, which we then use to define a log-normal prior on the effective temperature:

$$\mathcal{P}(\log T_{\text{eff}}|\text{colours}, [\text{Fe}/\text{H}]) = \mathcal{N}\left(\log T_{\text{eff}}, \frac{1}{2}(\log T_{\text{eff},84} - \log T_{\text{eff},16})\right)$$

conditional on the star's colour and $[\text{Fe}/\text{H}]$.

The posterior on T_{eff} , $\log g$, $[\text{Fe}/\text{H}]$, $[\alpha/\text{Fe}]$ and radial velocity was sampled for each star using the ensemble sampler `EMCEE` ([Goodman & Weare 2010](#); [Foreman-Mackey et al. 2013](#)) with 60 walkers for at least 2000 iterations. The first 1000 iterations of the chain were treated as burn-in and were discarded from the final posterior distribution. We verify the chain convergence by computing the Geweke scores ([Geweke 1992](#)) on each parameter and continue sampling until a satisfactory score is reached. We then use the chain to compute the best fit stellar atmospheric parameters and RVs. For most parameters we use and report the median and standard deviation from the posterior chains. The measured quantities and their uncertainties are validated in Section 4. As during the validation we observe that the uncertainties on the RV and $[\text{Fe}/\text{H}]$ are somewhat underestimated, we adjust them according to the validation results (see Sections 4.1.4.2). In Figure 5, we show examples of reduced 1D spectra together with the best-fit model templates.

Currently we fit the blue arm and red arm spectra with *rvspecfit* independently from each other. The results from the red arm spectra are used for most of the analysis work in this paper and will likely be the basis for the future *S*⁵ science papers. Furthermore, except for studying the repeatability of the measurements (e.g. in Section 4.1), we usually use the values from the spectrum with the highest S/N, when multiple observations were taken on a given object.

⁸ <https://github.com/segasai/rvspecfit>

⁹ <http://phoenix.astro.physik.uni-goettingen.de/>

¹⁰ *i*-band photometry is not used because no *i*-band observations were taken by DECaLS.

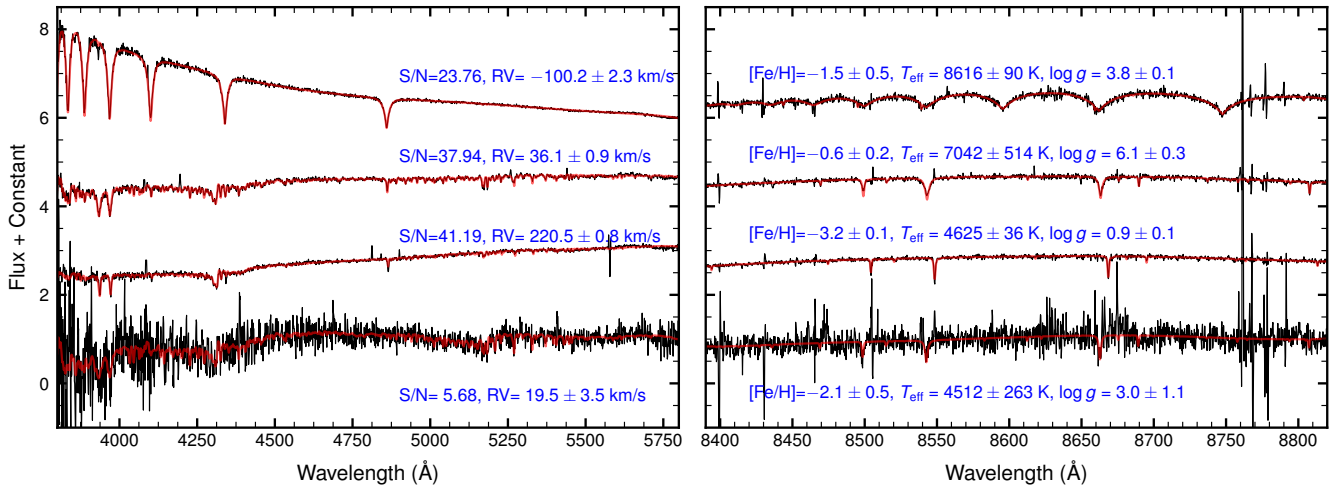


Figure 5. Examples of reduced 1D spectra from the blue arm (*left*) and red arm (*right*), spanning a range of S/N, [Fe/H], T_{eff} , and $\log g$ (black lines), over-plotted with the best fit model templates from RVSPECFIT (red lines). Best-fit parameters and uncertainties from the red arm spectra are shown. The y-axis represents the measured flux plus a constant offset for ease of visualization.

3.2.3 CaT Metallicity

In addition to RVSPECFIT, we determined the metallicities using the equivalent widths (EWs) of the CaT lines from the red arm spectra. This is an independent check on the metallicity measurements for the RGB stream members. We fit all three of the CaT lines with a Gaussian plus Lorentzian function. We then converted the summed EWs of the three CaT lines to [Fe/H] using the calibration relation as a function of absolute V magnitude from Carrera et al. (2013).¹¹ In order to derive the absolute magnitude of each star, the distance to the star is needed. Therefore, the CaT metallicity derived here are only valid for stream members where the distance to the stream is known. The uncertainties on the EWs are calculated uncertainties from the Gaussian and Lorentzian fit plus a systematic uncertainty of 0.2 Å added in quadrature. This systematic uncertainty is derived by checking the EWs from the repeated measurements (Li et al. 2017, 2018a), in a similar way as described in Section 4.1. The metallicity uncertainties are calculated from the uncertainties on the CaT EWs and the uncertainties on the calibration parameters from Carrera et al. (2013). Note that we do not include any uncertainty from the distance to the stars. Although distance uncertainties are usually reported with the paper announcing the discovery of the stream, a distance gradient is usually not initially determined, though it is present in most streams. A shift of 0.3 mag in distance modulus will cause a change in derived CaT metallicity of ~ 0.05 dex.

We note that the metallicity calibration relation from Carrera et al. (2013) only applies to RGB members and therefore the CaT metallicity derived here does not apply to stream members not on the RGB or to stream non-members.

3.2.4 Galaxy Redshifts

We independently determined redshifts of all blue arm spectra using AUTOZ (Baldry et al. 2014). While AUTOZ can in principle provide

the redshifts for all the stellar objects, it mainly focuses on determining accurate extragalactic redshifts. Therefore we only used the results from AUTOZ on non-stellar objects. All redshifts were visually inspected using MARZ (Hinton et al. 2016). Among the ~ 3000 targeted galaxies, ~ 2300 of them were observed when the moon is less bright and therefore have robust redshift measurements.

We found that a non-negligible fraction ($\sim 4\%$) of our stellar targets turn out to be QSOs based on the presence of broad emission lines. The QSO redshifts were measured using AUTOZ. Secure redshifts for 674 QSOs are presented in Table B1 of Appendix B. An additional 412 QSOs candidates were identified, but the limited spectral coverage included only a single broad emission line that could not be unambiguously identified. As QSOs are contaminants to our stellar sample, we removed QSOs using a photometric selection described in Section 4.4.

4 SURVEY VALIDATION AND QUALITY ASSURANCE

In order to assess the measurement quality of the S^5 pipeline, we observed several calibration fields during evening and morning twilight of the 2018 observing runs. These fields include a few globular clusters with metallicities ranging from -2.5 to -0.5 , and fields in the Sagittarius stream (see Table 2); targets in each field were selected from APOGEE (SDSS DR14; Majewski et al. 2017; Abolfathi et al. 2018) with magnitude range $12 < G < 16$. Since the targets are bright, the exposure time is less than 30 minutes for each field. The spectra were reduced and fit using exactly the same pipeline as described in Section 3.2.1 and 3.2.2. We then compared our derived parameters to the reported values to assess their accuracy. On top of dedicated APOGEE observations as validation we also use the measurements from LAMOST DR4 (Cui et al. 2012), Gaia-ESO Survey (GES) DR3 (Gilmore et al. 2012), SDSS/SEGUE (Allende Prieto et al. 2008) and GALAH DR2.1 (Buder et al. 2018) for stars from each survey that were serendipitously observed by S^5 . As the main science goals of S^5 are the stellar streams and Milky Way halo, we are mostly interested in the RVs and [Fe/H] measurements, thus we will focus on validating those two parameters in this section.

¹¹ We transformed from DES- g , r to V mag using equation (2) in Bechtol et al. (2015).

We note that the RVs and metallicities are derived independently from the blue arm and red arm spectra. For RVs, it is clear that the higher spectral resolution of the red arm should provide much better velocity precision for all but the bluest objects. For metallicities however, due to the much larger number of lines in the blue, as opposed to mostly CaT lines in the red, we expect the blue arm to be very competitive in abundance precision. However, we found that the red arm provides smaller systematic errors on metallicities at a cost of somewhat larger scatter. Therefore for the rest of the paper we mostly focus on the measurements from the red arm spectra for both RVs and metallicities. We may also use results from the blue arm spectra in the future, as they may be useful for some science cases (especially on bluer stars) and as a cross-check on the measurements from the red arm, and therefore we discuss more on blue arm spectra in Appendix C.

All RVs reported in this paper are heliocentric velocities after the barycentric motion of the Sun is corrected, unless otherwise noted.

4.1 Radial Velocity Validation

The validation of RVs consists of comparing the radial velocities to external catalogues as well as assessing repeated observations within S^5 .

The cross-match of the S^5 dataset with the APOGEE DR14 data contains ~ 800 stars and shows that the derived S^5 radial velocities have a systematic offset of 1.11 km s^{-1} .¹² A similar offset is seen in the comparison with *Gaia* DR2 RVs velocities, therefore we subtract this offset and define our final RVs as

$$v_{S5} = v_{rvspecfit} - 1.11 \text{ km s}^{-1}.$$

As mentioned earlier, some stream fields were observed more than once if the first observation was taken in poor weather. Some stars were also observed repeatedly when the AAT fields overlapped.¹³ We therefore are able to use those observations to assess the repeatability of RV measurements and the accuracy of RV uncertainties determined by the pipeline. Specifically, we consider all the pairs of repeated observations with RV uncertainties $\sigma_v < 30 \text{ km s}^{-1}$ and $S/N > 4$. We then model the pair-wise radial velocity differences $\delta v_{i,j} = v_i - v_j$ by a Gaussian model combined with an outlier model

$$\delta v_{i,j} \sim f \mathcal{N}\left(0, \sqrt{F(\sigma_{v,i})^2 + F(\sigma_{v,j})^2}\right) + (1-f) \mathcal{N}(0, \sigma_{out})$$

where $\sigma_{v,i}, \sigma_{v,j}$ are the RV uncertainties of the i -th and j -th observation respectively and $F(\sigma_v) = \sqrt{\sigma_{v,floor}^2 + (k \times \sigma_v)^2}$ is the uncertainty transformation function. Here k is the scaling factor for the RV uncertainty and $\sigma_{v,floor}$ is the systematic floor of radial velocity precision. We fit the model to ~ 3500 repeated observations and find $k = 1.28$ and systematic floor is $\sigma_{v,floor} = 0.66 \text{ km s}^{-1}$. Thus our final RV uncertainties are determined as

$$\sigma_{v,S5} = \sqrt{(1.28 \sigma_{v,rvspecfit})^2 + 0.66^2}$$

We note that the likely reason for the presence of the systematic floor in RV determination is the accuracy of the 2dF/AAOmega

¹² The cause of the offset is not yet clear and is likely related to either wavelength calibration bias, template mismatches or asymmetries in the line-spread function.

¹³ This is because AAT has a FOV slightly larger than 2° in diameter.

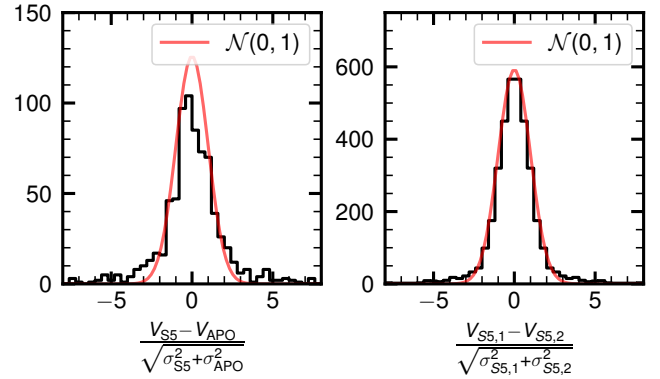


Figure 6. Comparison of S^5 radial velocities with APOGEE and repeated observations. *Left panel:* The black histogram shows the distribution of differences of the S^5 RVs and APOGEE RVs normalised by the combined uncertainty of S^5 and APOGEE ($\sqrt{\sigma_{APO}^2 + \sigma_{S5}^2}$). The red line shows the Gaussian distribution with zero mean unit variance. The stars included for comparison have $(G_{BP} - G_{RP})_0 < 1.5$, small RV scatter in APOGEE $v_{scatter} < 0.5 \text{ km s}^{-1}$, $(S/N)_{S5} > 4$, and $\sigma_{S5} < 20 \text{ km s}^{-1}$. *Right:* The distribution of pairwise RV differences from S^5 repeated observations divided by the combined uncertainty $\sqrt{\sigma_{S5,1}^2 + \sigma_{S5,2}^2}$. The red curve shows the $\mathcal{N}(0, 1)$ distribution that well describes the observations. We only show the stars with $\sigma_{v,S5} < 30 \text{ km s}^{-1}$ and $S/N > 4$.

wavelength calibration. The multiplicative constant in the radial velocity uncertainty is not equal to 1 probably because of the covariance between pixels in the reduced spectra (produced naturally as a result of various rebinning/resampling steps of the 2dF pipeline). We find that the correlation coefficients of the noise between neighbouring pixels in the spectra are ~ 0.3 . If this covariance in the noise is ignored as it is in the current analysis, this is expected to produce underestimated uncertainties by $\sim 30\%$, similar to what we empirically determine.

We demonstrate the performance of the recalibrated RVs and uncertainties in Figure 6. In the left panel we compare the S^5 RVs with APOGEE RVs (using the `vhelio_avg` column) by showing the distribution of S^5 and APOGEE RV differences normalized by the combined uncertainty $\sqrt{\sigma_{v,S5}^2 + \sigma_{v,APO}^2}$. For the plot we use the APOGEE/ S^5 stars that have high enough $S/N > 4$, small RV errors ($\sigma_{S5} < 20 \text{ km s}^{-1}$ in S^5), and do not show significant RV variation in APOGEE ($v_{scatter} < 0.5 \text{ km s}^{-1}$). Since the APOGEE sample is dominated by red and cool objects, while the S^5 targets are significantly bluer on average, we additionally restrict our APOGEE/ S^5 sample to stars with $(G_{BP} - G_{RP})_0 < 1.5$, which includes the majority of stars (95%) in S^5 . If the uncertainties of the S^5 RVs are correct and there are no residual RV systematics, the distribution shown on the left panel of Figure 6 should behave like a $\mathcal{N}(0, 1)$ Gaussian. The distribution is indeed centred at zero, with the core of the distribution similar to the $\mathcal{N}(0, 1)$; however, more extended tails are also visible. The extended tails are likely caused by: (1) template mismatches and RV shifts related to convection or gravitational redshifts that can reach the level of $\sim 0.5 < \text{km s}^{-1}$ (Allende Prieto et al. 2013; Zwitter et al. 2018); (2) stellar binarity. While we remove stars that show RV variability in APOGEE $v_{scatter} > 0.5 \text{ km s}^{-1}$, it is likely that our sample contains longer period binaries with RV changes between the APOGEE and S^5 observations.

The right panel of Figure 6 assesses the repeatability of the

radial velocities and correctness of the RV uncertainties by showing the distribution of pairwise RV differences in S^5 divided by the combined uncertainty. Here the distribution is very close to the normal distribution with zero mean and unit variance, confirming the correctness of our error model and RV stability of our measurements.

In this section we described the validation of radial velocities determined from the red arm (1700D) that are used for the majority of the targets. We briefly discuss the same procedure for determining the zero-point offset and the error model of the blue arm (580V) RVs in Appendix C.

4.2 [Fe/H] validation

To validate the S^5 [Fe/H] measurements we compare them with APOGEE, GALAH, GES, LAMOST and SEGUE survey data. We highlight that the [Fe/H] measurements are expected to be much more affected by systematic errors related to the stellar atmospheres/spectral templates used rather than purely random errors. Those systematic biases are also potentially different for stars with different atmospheric parameters, therefore we do not try to correct them but instead assess the overall quality of [Fe/H] measurements.

First we adopt the same scaling for the [Fe/H] uncertainties as for the RVs, as it is caused by correlated noise in the spectra.

$$\sigma_{[\text{Fe}/\text{H}],S^5} = 1.28 \times \sigma_{[\text{Fe}/\text{H}],\text{rvspecfit}}$$

This scaling also guarantees that repeated measurements of [Fe/H] are consistent within the error (similar to right panel of Figure 6).

We start by looking at the comparison of the [Fe/H] from RVSPECFIT (from the red arm spectra) with the APOGEE [Fe/H]. We select the set of stars with both APOGEE and S^5 measurements similar to the one used in Section 4.1, but on top of that we also require that none of the STAR_WARN or STAR_BAD bits from APOGEE are set and that the $T_{\text{eff,APO}} > 4300\text{K}$, as we notice that for very cool stars (that are not representative of the S^5 targets) our pipeline produces a bias in the effective temperature and a bias in [Fe/H]. With this caveat in mind we compare with APOGEE abundances. The left panel of Figure 7 shows the APOGEE metallicities vs S^5 metallicities. We remark that our metallicities track those from APOGEE, but with some occasional systematics; i.e. for very high metallicities ($[\text{Fe}/\text{H}] > 0.2$), there is a possible bias towards higher values (near $[\text{Fe}/\text{H}] \approx -1$). But overall the agreement is good with the systematic errors mostly below $\sim 0.2 - 0.3$ dex and scatter of the same magnitude.

Since the APOGEE dataset is dominated by metal-rich giants we also compare the S^5 measurements with various large high and low resolution surveys such as LAMOST, GALAH, GES and SEGUE. This is shown on the right panel of the Figure 7. Here we can see that with the additional surveys we get a much better sampling of the metal poor end of the stellar metallicity distribution, and we see no evidence of a significant metallicity bias. We note that there are some catastrophic outliers in the data as well. Overall the summary of our metallicities with respect to various surveys as measured by the median deviation and half of the difference between 84th and 16th percentiles is $\{-0.18, 0.34\}$ for GES, $\{0.10, 0.33\}$ for GALAH, $\{-0.04, 0.25\}$ for LAMOST, and $\{0.09, 0.31\}$ for SDSS/SEGUE and $\{-0.02, 0.21\}$ for APOGEE.

4.3 Comparison with MIKE Spectroscopy at the metal-poor end

Although we have shown the metallicity from S^5 is in good agreement with other surveys, the comparison set is largely metal-rich, while the stellar streams and stellar halo mostly consist of metal-poor stars. To verify the metallicity measurements from S^5 are robust on the most metal-poor stars in our sample, we observed a subset of the brightest stars ($g \lesssim 17$) with the high-resolution MIKE spectrograph (Bernstein et al. 2003) on the Magellan/Clay Telescope. MIKE targets were selected to be either stream members identified by S^5 or the extremely metal-poor star candidates from AAT metallicity of $[\text{Fe}/\text{H}] \lesssim -3.5$.

We observed our MIKE targets on 29-30 Sep 2018 with the 0''.7 slit in good weather, providing $R \sim 30,000$ and $\sim 40,000$ on the red and blue arms, respectively. Data were reduced with the CARPY MIKE pipeline (Kelson 2003)¹⁴. Radial velocity measurement, continuum normalization, and equivalent widths of Fe I and Fe II lines were measured with a new version of the SMH analysis environment first described in Casey (2014)¹⁵. A standard 1D LTE analysis was performed, using the ATLAS stellar atmospheres (Castelli & Kurucz 2003) and the MOOG radiative transfer code updated to include scattering (Snedden 1973; Sobeck et al. 2011)¹⁶. The effective temperature and microturbulence were determined by balancing the Fe I abundance vs. excitation potential and reduced equivalent width, respectively. The surface gravity was set by balancing the Fe I and Fe II abundances. Following Frebel et al. (2013), we then corrected the effective temperature to match the photometric effective temperature scale (which for cool metal-poor giants typically increases [Fe/H] by ≈ 0.2 dex), and readjusted the surface gravity and microturbulence accordingly. Statistical uncertainties were estimated from the error in the slopes for effective temperature and microturbulence, and combined standard error on the mean for surface gravity. We adopt the standard deviation of Fe I abundances as the [Fe/H] uncertainty. Typical systematic uncertainties are 150 K, 0.3 dex, 0.2 km s⁻¹, and 0.1 dex for effective temperature, surface gravity, microturbulence, and metallicity, respectively (see Ji et al. 2019 for details).

Here we are mostly interested in validating S^5 metallicities of the most metal-poor stars and therefore we only focus on the comparison of the metallicities from MIKE observations and from AAT observations. A full abundance analysis of other elements as well as the scientific interpretation of this data set will be presented in future work.

Figure 8 shows the metallicity measurements from MIKE in comparison with the AAT observations. The left panel shows the metallicities derived from RVSPECFIT template fitting method with all MIKE targets. Despite a large metallicity range from $-4 \lesssim [\text{Fe}/\text{H}] \lesssim -1.5$, the metallicities from the two independent measurements are in good agreement. In the right panel of the Figure, we compare with the CaT metallicities from AAT observations (Section 3.2.3). Since CaT metallicities require the distance of the star as an input, only stream members are shown. The $[\text{Fe}/\text{H}]_{S^5,\text{CaT}}$ vs. $[\text{Fe}/\text{H}]_{\text{MIKE}}$ metallicity show a tighter sequence with an *rms* of 0.18 dex than the $[\text{Fe}/\text{H}]_{S^5,\text{RVSPECFIT}}$ vs. $[\text{Fe}/\text{H}]_{\text{MIKE}}$ with an *rms* of 0.3 dex.

We therefore conclude that the metallicities derived from

¹⁴ <http://code.obs.carnegiescience.edu/carnegie-python-distribution>

¹⁵ <https://github.com/andycasey/smhr>

¹⁶ <https://github.com/alexji/moog17scat>

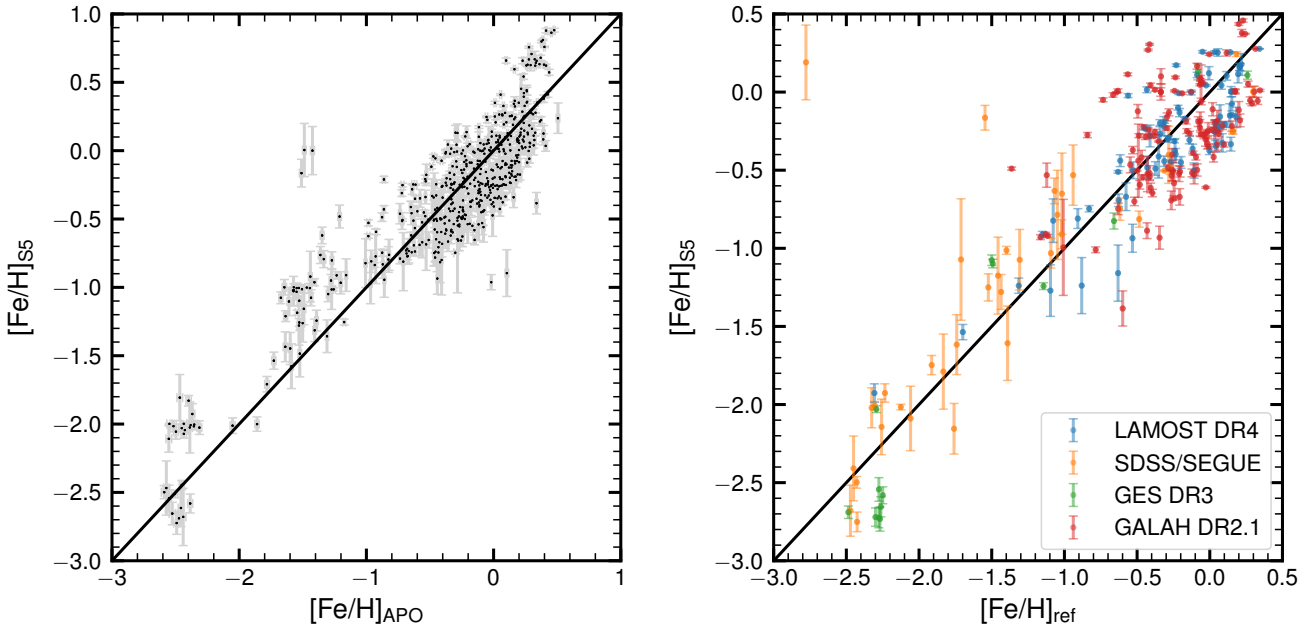


Figure 7. Comparison of the S^5 spectroscopic metallicities from `rvspecfit` with APOGEE (*left*) and other surveys (*right*). We only use stars with $(G_{BP} - G_{RP})_0 < 1.5$, $S/N > 4$ and $\sigma_{[Fe/H],S^5} < 0.5$. The left panel additionally excludes the APOGEE stars with effective temperatures below $T_{\text{eff}} = 4300$ K. The right panel shows the comparison with various large spectroscopic survey datasets that were mostly serendipitously observed by S^5 . We notice that despite a few outliers and a spread of ~ 0.3 dex there is a very good one-to-one mapping between our measurements and those from other surveys.

`rvspecfit` are generally reliable even at the most metal-poor end. However, if the distance of the star is known, the CaT metallicity exhibits smaller scatter. In future studies on stellar streams, CaT metallicities will be considered when available.

4.4 QSOs in S^5

During the visual inspection of galaxy redshifts as described in Section 3.2.4, we found that our stellar sample contains a large (> 1000) population of QSOs.

To efficiently identify QSOs in the S^5 data, and remove them from stellar analyses, we use the combination of the WISE data with *Gaia* DR2 data, as they are known to be highly efficient for selecting QSOs (see e.g. Wright et al. 2010; Lemon et al. 2017). We crossmatch all the targets with the unWISE catalogue that combines the data from the original WISE mission and NEOWISE (Schlafly et al. 2019). Figure 9 shows the *Gaia*-WISE colour $G - W1$ vs $W1 - W2$ colour distribution of all S^5 targets, where the colour-coded symbols indicate objects that have been labeled as QSOs from visual inspection of the spectra and have measured redshifts, while grey dots show all other objects in S^5 . The colours of the QSO symbols correspond to the QSO redshift ($0.5 \lesssim z \lesssim 2.5$). It is clear that the QSOs occupy a well defined area of colour space, therefore for the stellar analysis we exclude all the objects lying above the broken line in the Figure defined as:

$$(W1 - W2) > \text{Max}(0.5, 0.5 - (G - W1 - 2.75)) \quad (4)$$

which selects ~ 1700 QSO candidates in the current S^5 sample. We note that fewer than 10 out of ~ 1100 spectroscopically identified QSOs lie outside of our QSO selection area. For the spectroscopically identified QSOs with robust redshift measurement, we provide their redshifts in the table of Appendix B.

4.5 Selection of good quality stellar spectra

The S^5 data set spans a very large range of signal-to-noise, and includes contamination from galaxies, QSOs, and sometimes rare object types. We therefore need a way of identifying low quality, poorly fit stellar spectra or non-stellar spectra without individually examining each spectrum. One way to do that is to define a threshold in the S/N , uncertainty in RV, and/or chi-squared values of the template fit. However, these are difficult criteria to define, since a high-metallicity cool star may have a good velocity determination even at very low S/N while a hot and/or metal-poor star may not get an RV measurement even at $S/N=10$. Furthermore, at high S/N the template mismatch to stellar spectra is very prominent (leading to high chi-squared values) while at low S/N the sky line residuals can be very significant in the 1700D spectra. Therefore we train a random forest classifier (RFC; Breiman 2001) to identify good-quality stellar spectra. We fit it separately to the red and blue arm spectra. The parameters that we use as features are the chi-squared values of the fit, radial velocity error, radial velocity posterior skewness and kurtosis, effective temperature, median signal to noise in the spectrum and relative median absolute deviation from the best fit template model $\text{Median}(|\text{Spec-Model}|)/\text{Median}(\text{Spec})$. The classifier is trained to identify good quality spectra, that were labeled using a $|\text{RV}| < 500 \text{ km s}^{-1}$ criterion, because many non-stellar or low quality and S/N objects are spuriously assigned to larger radial velocities up to the very edge of the considered range of 2000 km s^{-1} . The RFC returns a probability of being a good stellar spectrum. This does not guarantee that all the stellar parameters are trustworthy, but provides a base selection of very likely stars with reliable RV. We then create a binary (0/1) flag `GOOD_STAR` and set it to 1 for those with the RFC good spectrum probability > 0.5 . Finally, we set `GOOD_STAR = 0` for all objects that are identified as QSOs based

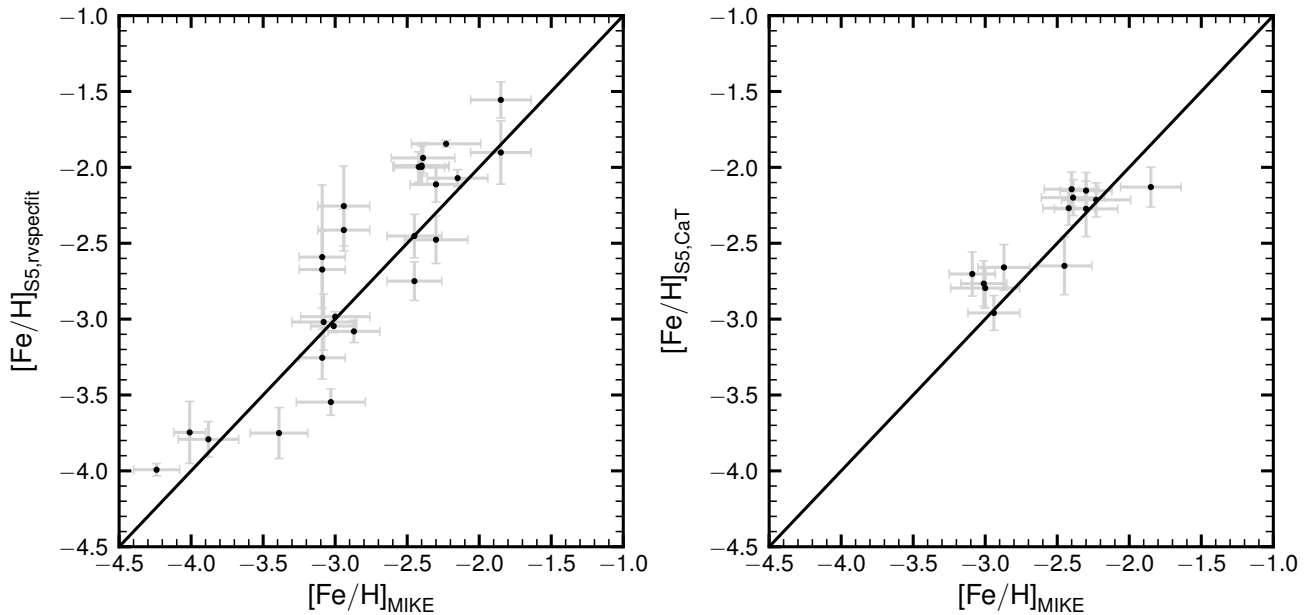


Figure 8. Comparison of the metallicities from AAT observations with MIKE spectroscopy for a subset of stream member stars and extreme metal-poor candidate stars. The left and right panels show the AAT metallicities derived from `rvspecfit` and the CaT lines, respectively. Since the CaT metallicity requires distance as input, only stream members are shown. CaT metallicities in general show a tighter sequence to the MIKE metallicities than the `rvspecfit` metallicity.

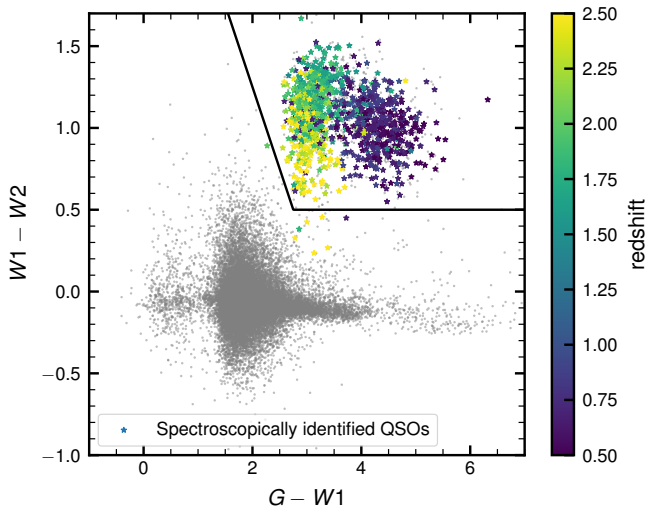


Figure 9. The *Gaia*-WISE colour-colour plot showing all the S^5 targets with coloured star symbols marking the subset of objects that were spectroscopically identified as QSOs. The colour indicates the redshifts. The broken solid line denotes the boundary (Eq. 4) that we adopt to reject the QSOs in the stellar analysis.

on their WISE-*Gaia* photometry in Section 4.4 and galaxy targets in Section 3.2.4 as non-stellar objects.

The `GOOD_STAR` flagging removes both the non-stellar spectra and the stellar spectra with bad measurements (e.g., low S/N, etc.). We use the `GOOD_STAR = 1` for the stellar-related science discussion in Section 5. We note, however, the selection might be chosen differently for future science paper upon the science goals.

5 EARLY SCIENCE RESULTS

5.1 Stream Results

The primary goal of the S^5 survey is to confirm the newly discovered streams kinematically, as well as to measure the RVs and metallicities of the streams to understand their orbits, evolution, progenitors, etc. While we will provide more detailed studies of individual streams in future papers, here we give a brief overview of the stream kinematics based on the S^5 data collected so far. We focus on the DES streams since none of them were previously observed or confirmed spectroscopically.

As shown in Figure 1, among all the DES streams that have been observed, Tucana III was observed entirely before S^5 and published in Li et al. (2018b); Turrana has only one field observed so far; the other nine streams have been mostly covered in 2018.

Figure 10 provides the summary of the stream kinematics as seen by S^5 . We plot the heliocentric RVs of the targeted stars as a function of declination for seven streams, for which we see a clear kinematic signal (i.e. clustering in RV and a coherent change in RV as a function of declination). These seven streams are Aliqa Uma, ATLAS, Chenab¹⁷, Elqui, Indus, Jhelum, Phoenix. For the other two streams, Ravi and Willka Yaku, the member association does not immediately stand out, and further investigations or observations are needed.

Figure 10 highlights the abundance of cold substructure present in the Milky Way halo. The sample of stars plotted in Figure 10 has been selected using proper motion and photometric information and

¹⁷ Here we treat Chenab and Orphan Stream separately although Koposov et al. (2019b) have shown that they are essentially one stream. We only show the stream targets in Chenab that are inside the DES footprint. A future paper will present all S^5 observations on Chenab+Orphan.

has no RV selection applied. RV measurements from S^5 produce a highly structured picture with individual streams clearly resolved. In future papers, we will investigate these streams in more details. In particular, two streams, the ATLAS stream and the Aliqa Uma stream (at $\delta_{2000} \sim -35^\circ$ to -20° in Figure 10), which were previously thought to be independent, are in fact a single stream from phase space information (Li et al. in prep).

5.2 BHB/BS Separation with *griz* colour

Old, metal-poor BHB stars have bright absolute magnitudes and are robust distance indicators, and thus are ideal tracers of the Milky Way’s stellar halo (Deason et al. 2011, 2012). In SDSS, multi-band photometry has been used to select BHB stars (see e.g., Yanny et al. 2000; Deason et al. 2011). The selection relies on the $u - g$ colour, which provides a subtle distinction between BHB stars and blue straggler (BS) stars¹⁸ at similar temperature but higher surface gravity. However, DES and many other ongoing imaging surveys (e.g. Hyper Supreme Cam, DECaLS, etc) do not include u -band photometry. Recent work has shown that a combination of *griz* photometry alone can also differentiate BHB stars from BSs (see e.g., Vickers et al. 2012; Belokurov & Koposov 2016; Deason et al. 2018). Here, we use the stellar parameters measured from S^5 to show clear BHB and BS sequences separated with DES DR1 photometry.

We select all stars in S^5 with $-0.4 < (g - r)_0 < 0.1$ (mostly from the P6 target class) and $6000 < T_{\text{eff}} < 10000$ K as BHB candidates. In addition, we require `GOOD_STAR = 1` and the S/N of the red arm spectra > 5 to remove QSOs as well as to ensure the stellar parameters are reliable. We then show in Figure 11 that the BHBs and BSs are clearly distinct in (1) stellar parameters $\log g - T_{\text{eff}}$ space (left panel), (2) $(g - r)_0$ vs $(i - z)_0$ photometric space (right panel), and (3) kinematic space (colour coding). For the kinematics, we calculated the absolute value of the 3D heliocentric velocity v_{3D} of each star based on the proper motion from *Gaia*, RV from S^5 , and the heliocentric distance assuming that the star is a BHB.¹⁹ Therefore, v_{3D} for BHBs is correct, while for most BSs that are intrinsically fainter and therefore closer, the inferred v_{3D} is expected to be inflated by a factor of 2-3. This can be seen in the colour scale of the left panel of Figure showing that high $\log g$ stars have high inferred v_{3D} , further confirming that the stellar parameters from S^5 are robust to, e.g., separate the BHBs from BSs. We then select stars above the solid line in the stellar parameter space (left panel) as BHBs (triangle symbols), and stars below as BS (star-shaped symbols). These two populations show almost perfect separation in the colour–colour space in the right panel. The tight BHB sequence in $(g - r)_0$ vs $(i - z)_0$ allows high purity BHB selection with DES DR1 for any potential studies on the Milky Way halo.

To make it is easier for future studies of BHBs we determine the curve that best separates the BHB from BS:

$$(i - z)_0 = 1.11371(g - r)_0^5 - 1.50963(g - r)_0^4 + 0.94966(g - r)_0^3 + 0.29969(g - r)_0^2 + 0.20021(g - r)_0 - 0.03684 \quad (5)$$

This curve is shown by a dashed line on Figure 11, with BHB lying

¹⁸ We note that we call all of the hot dwarfs BSs here but in principle some of them could be hot young main-sequence stars as well.

¹⁹ The distance is derived using the BHB absolute magnitude relation M_g vs $g - r$ in Belokurov & Koposov (2016).

above, and BS below the curve. We have determined this function by fitting for the polynomial providing the maximum margin separation in $(i - z)$ between BHB and BS classes (see e.g. section 7.1.1 of Bishop 2006). As the separation between BHB and BS is also observed in the space of $g - r$ and $r - z$ colours, and surveys like DECaLS (Dey et al. 2019) do not observe in the i -band, we provide a boundary relying on g, r, z filters alone:

$$(r - z)_0 = 1.07163(g - r)_0^5 - 1.42272(g - r)_0^4 + 0.69476(g - r)_0^3 - 0.12911(g - r)_0^2 + 0.66993(g - r)_0 - 0.11368 \quad (6)$$

Both panels of Figure 11 also show the *Gaia* RR Lyrae (marked by red circles) that were targeted by S^5 . They are naturally scattered across the $(g - r)_0$ vs $(i - z)_0$ space due to variability, while mostly occupying a tight corner in stellar parameter space (low $\log g$ and $T_{\text{eff}} \lesssim 7500$ K).

We note that there are ~ 400 BHB stars plotted in Figure 11 (with an additional ~ 400 BSs). In total, there are about 700 BHBs observed in S^5 (defined as $6500 < T_{\text{eff}} < 10000$ K and above the solid line in the left panel of Figure 11). Among the ~ 300 BHBs not shown in the Figure, about half are outside of DES footprint and therefore no *griz* photometry is available, while the other half have $S/N < 5$ in the red arm spectra. This BHB dataset is valuable for studies of the kinematic properties of the Milky Way halo, including measuring the potential of the Milky Way (Deason et al. 2012), studying the wake from LMC infall (Garavito-Camargo et al. 2019; Belokurov et al. 2019), and understanding the remnants from *Gaia* Sausage in the outer halo (e.g., Lancaster et al. 2019).

5.3 Photometric Metallicity in *griz* colour

The broadband colours of stars are sensitive to the metallicity of the stars. The metallicity of a metal-poor star can usually be estimated via the ultraviolet (UV) excess, i.e. the difference between the star’s $U - B$ colour and that which would be measured for a more metal-rich star with the same $B - V$ colour, (see, e.g., Wildey et al. 1962; Sandage 1969). Ivezić et al. (2008) showed that the photometric metallicity of F/G stars could be estimated from the position of stars in the SDSS $u - g$ vs $g - r$ diagram. Unfortunately, DES does not routinely use the DECam u -band. However, Li et al. (2018b) showed that metal-poor stars at $(g - r)_0 > 0.4$ are separable from metal-rich stars of the same $g - r$ colour using the $g - r$ vs $r - i$ colour combination instead. Here, we examine the correlation between the metallicity and broadband photometry in *griz* with the stellar metallicities from S^5 data.

We select stellar targets with `GOOD_STAR = 1`, $S/N > 5$, $\sigma_{[\text{Fe}/\text{H}]} < 0.5$ from S^5 to ensure that the sample has reliable metallicity measurements with small uncertainties. We limit this analysis to stars in DES footprint, which have *griz* photometry from DES DR1. In Figure 12, we show the correlation of the stellar metallicity with the position of a star in the $(g - r)_0$ vs. $(r - i)_0$ diagram. The colour scheme shows the average metallicity value in each bin. At $0.4 < (g - r)_0 < 0.8$, it is obvious that at a constant $(g - r)_0$ colour, metal-poor stars tends to have redder $(r - i)_0$ colours. At $(g - r)_0 < 0.4$, the separation becomes weaker and therefore it is harder to assess the metallicity of MSTO stars with *gri* colour alone. A similar trend is also shown in the $(g - r)_0$ vs. $(r - z)_0$ diagram and therefore this correlation could be applied to DECaLS data, which lacks i -band observations, as well. In the future, photometric metallicities could be derived for the entire DES and DECaLS data

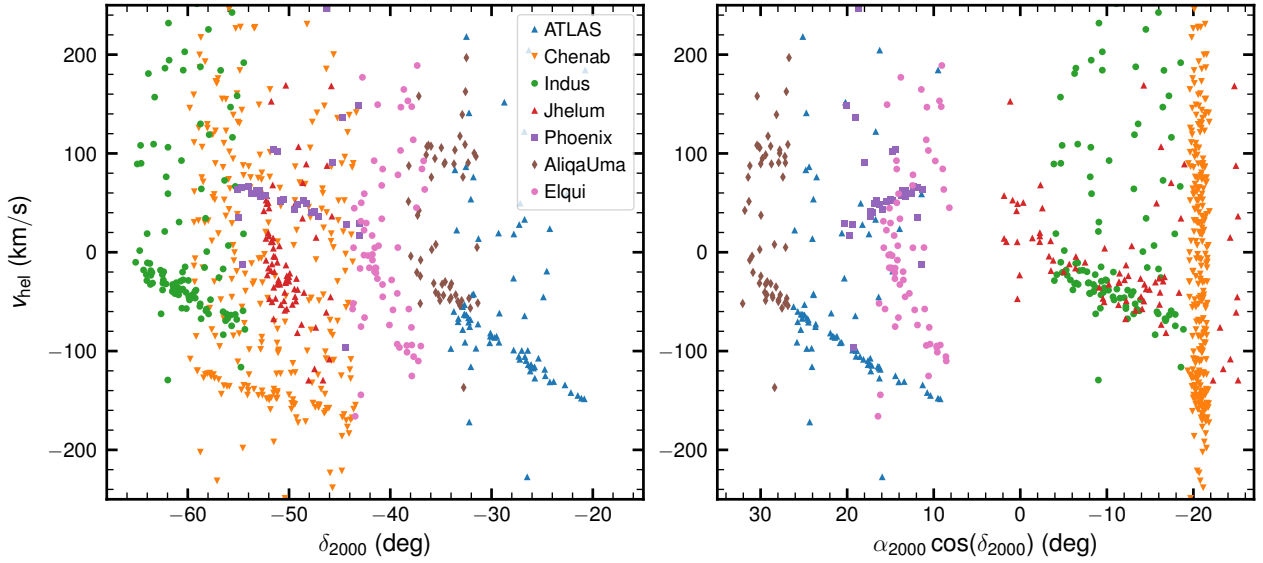


Figure 10. Heliocentric RV as a function of declination (δ_{2000} , left) and right ascension corrected by declination ($\alpha_{2000} \cos(\delta_{2000})$, right) for stream target stars, colour coded for different stream fields. Seven streams with clear signals of stream members (i.e. clumpiness in RV) are shown. Plotting only high priority (P9) targets with $\log g < 4.1$ and $[\text{Fe}/\text{H}] < -1$ and no radial velocity cuts, the stream members are immediately visible.

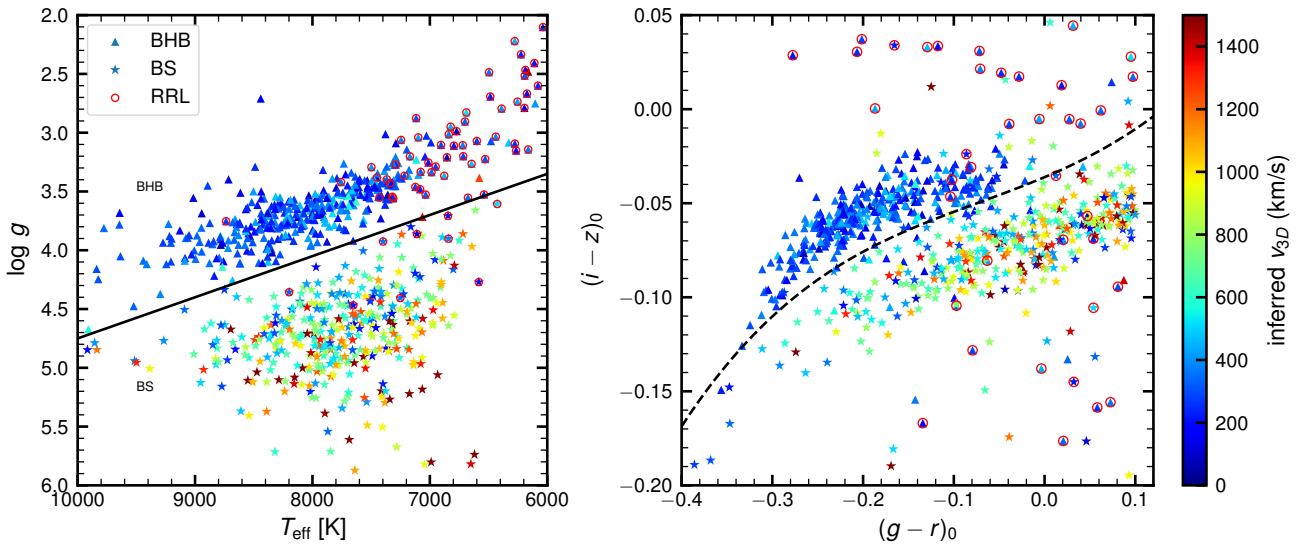


Figure 11. *Left panel:* The distribution of blue stars ($-0.4 < (g-r)_0 < 0.1$) in spectroscopic parameter $\log g - T_{\text{eff}}$ space. We can clearly see the separation between BHB and BS stars. We define our BHB (triangle symbols) and BS (star symbols) sample as stars below/above (respectively) the relation $\log g = 1.25 + 0.35 \frac{T_{\text{eff}}}{1000}$ shown by a black solid line. *Right panel:* The colour-colour distribution of S^5 blue stars. Thanks to the high photometric precision of DES DR1, BHBs and BSs are well separated in the dereddened $g-r$ vs $i-z$ diagram. In both panels, all stars are colour-coded with the absolute value of their 3D heliocentric velocities, calculated with their distance based upon the assumption all of the stars are BHBs. Therefore, their 3D velocities should be correct for the BHBs and inflated for the BSs. This effect is seen in the stellar parameter space (left panel) and colour-colour space (right panel). The dashed curve on the right panel shows the polynomial in $(g-r)_0$ vs. $(i-z)_0$ that we propose to separate BHB from BS using photometry only (see Eq. 6). In addition, we identify the targeted RR Lyrae (RRL) stars from *Gaia* DR2 by open red circles in both panels. Although the BHBs and BS follow tight sequences in the colour-colour diagram, RRLs are scattered in colour depending on their phase at the time of observation, but are well clustered at $2 \lesssim \log g \lesssim 4$ and $6000 < T_{\text{eff}} < 7500$ in $\log g - T_{\text{eff}}$ space.

sets, enabling statistical studies of the metallicity distribution of the Milky Way's stellar halo.

5.4 Metallicity Distribution Function in S^5

The S^5 target selection preferentially selected metal-poor halo stars, resulting in a large sample of stars with low metallicities. In Figure 13, we show the raw metallicity distribution function (MDF) from S^5 , after applying quality cuts of $\text{GOOD_STAR} = 1$, $\text{S/N} > 5$

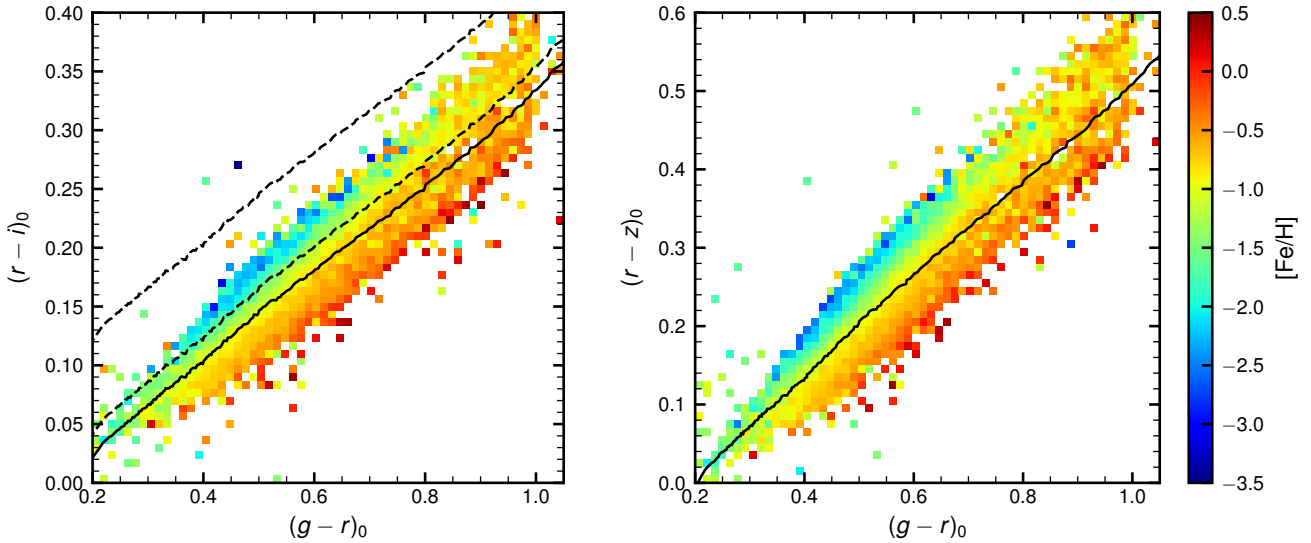


Figure 12. *Left panel:* 2D histogram in dereddened $g-r$ vs $r-i$ diagram, colour coded with the mean metallicity in each bin, obtained by S^5 . The solid line shows the stellar locus in DES. The dashed lines shows the boundary of the selection of metal-poor stars (P4 targets in Section 2.3.5). As discussed in the target selection for both streams and metal-poor stars, high precision DES DR1 photometry easily separates metal-rich stars from the metal-poor stars, with more metal-poor stars being located to the upper left of the stellar locus. Therefore, a photometric metallicity can be obtained based on $griz$ colour. Note, however, that such separation disappears at $(g-r)_0 \lesssim 0.4$ and therefore is not applicable to MSTO stars. *Right panel:* same plot but in dereddened $g-r$ vs $r-z$ space. Similar (and probably better) correlation between stellar metallicity and colours is visible.

and $\sigma_{[\text{Fe}/\text{H}]} < 1$. In this sample, about 37% (6%) of the 22k stars have $[\text{Fe}/\text{H}] < -1$ ($[\text{Fe}/\text{H}] < -2$); ~ 190 stars are at $[\text{Fe}/\text{H}] < -3$, of which ~ 90 are brighter than $g_0 < 17.5$. As an initial comparison, we show the raw MDFs from the Hamburg-ESO survey (HES, Schörck et al. 2009) and the metal-poor star survey by Yong et al. (2013). The overall number of metal-poor stars in S^5 is comparable to these previous surveys, though the S^5 stars are fainter and may thus probe farther into the halo. These raw star counts should not be compared to models, since selection effects are extremely important (see dashed line in right panel of Figure 13). Future work quantifying the S^5 selection function should provide interesting constraints on the Milky Way’s MDF.

6 CONCLUSIONS AND FUTURE WORK

In this paper we present the Southern Stellar Stream Spectroscopic Survey (S^5), targeting the kinematics and chemistry of stars in prominent tidal streams in the Galactic halo. The S^5 survey design combines observations of stellar streams, the primary objective of S^5 , with auxiliary observations of various Milky Way halo tracers and low-redshift galaxies. We show, by comparing our measurements with APOGEE and other spectroscopic surveys, that the S^5 radial velocities and stellar metallicities are robust.

As of June 2019, we have observed 110 AAT fields (~ 3 deg² per field), of which 70 fields are in the DES footprint. We observed nine DES streams along $> 80\%$ of their length. When combined with the previously published Tucana III stream, the S^5 data represent the first spectroscopic measurements of ten out of fourteen DES streams. Among the nine newly observed streams, we have confirmed at least seven of them as genuine streams in phase space, with each of them displaying small velocity dispersion (Figure 10). The observed velocity distribution of S^5 demonstrates that the Milky Way stellar halo is rich in substructure. Some of the structures that are not easily associated with each other based on

positions on the sky line up in phase space, suggesting a common origin. This emphasizes the crucial role the upcoming spectroscopic surveys (such as WEAVE, DESI, 4MOST, SDSS-V; Dalton et al. 2012; DESI Collaboration et al. 2016; de Jong et al. 2012; Kollmeier et al. 2017) will play in the mapping and untangling the Milky Way’s stellar halo.

So far, S^5 has collected 43k spectra on 38k unique targets, of which 3k are targeted as low- z galaxies, and the rest are targeted as stars.²⁰ Among 38k unique targets, 33k/25k/14k/5k of them have $S/N > 2/5/10/20$ per pixel (~ 0.23 Å/pixel) in the red arm spectra. 31k out of 38k spectra have `GOOD_STAR = 1` (see definition in Section 4.5) and can be further used for stellar related science analysis.

In addition to the primary science goals related to stellar streams, S^5 has also collected spectra for a number of other targets that could potentially deliver interesting science results. For example,

- ~ 400 RR Lyrae candidates were targeted, of which ~ 340 have good spectra.
- ~ 150 white dwarf candidates were observed.
- ~ 190 stars have measured $[\text{Fe}/\text{H}] < -3$, of which ~ 90 have $g_0 < 17.5$.
- ~ 700 BHBs were identified (see Section 5.2).
- One of the fastest hyper-velocity stars in the Galaxy (with a Galactocentric velocity of > 1700 km s⁻¹) was discovered and associated with the ejection from the Galactic Centre (Koposov et al. 2019a).
- ~ 1700 photometrically identified QSOs were observed, of which 640 have robust redshift measurements (see Section 4.4 and Appendix B for details).
- ~ 3000 galaxy targets were observed, of which ~ 2300 have

²⁰ However, 1.7k of the stellar targets turned out to be QSOs; see Section 4.4.

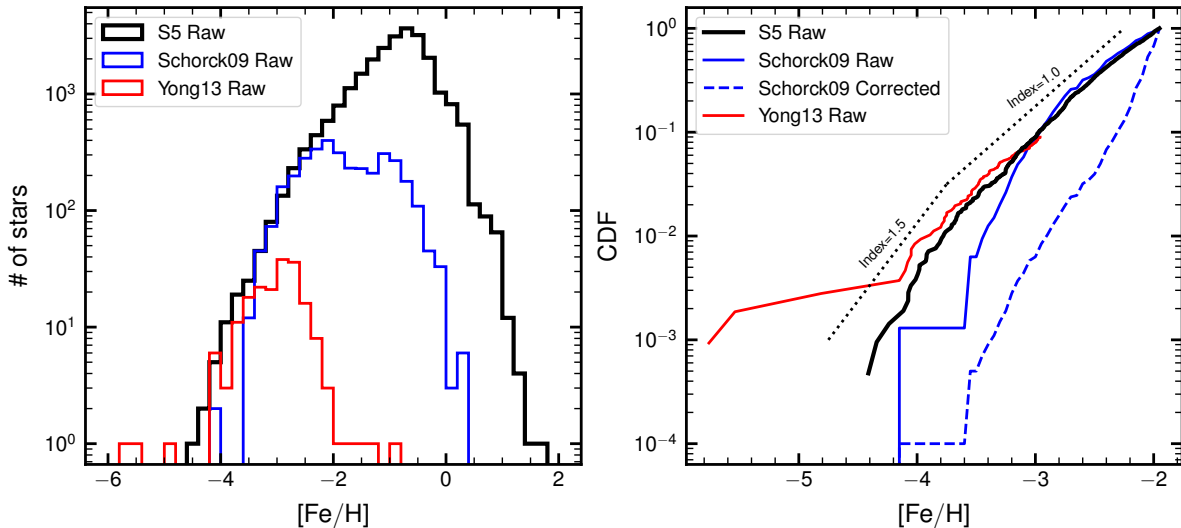


Figure 13. *Left panel:* Raw metallicity distribution function (MDF) from S^5 , compared to the HES (Schörck et al. 2009) and a metal-poor star survey (Yong et al. 2013). S^5 has identified a comparable number of $[\text{Fe}/\text{H}] < -3$ stars and slightly more $[\text{Fe}/\text{H}] < -4$ than HES. *Right panel:* cumulative density functions (CDF) for S^5 , HES, and Yong et al. (2013). The Yong et al. (2013) CDF only includes stars with $[\text{Fe}/\text{H}] < -3$, and has been rescaled to match S^5 at $[\text{Fe}/\text{H}] = -3$. Power law indices of 1.0 and 1.5 are shown for comparison. The dashed blue line shows the true MDF inferred by Schörck et al. (2009) after accounting for selection effects.

robust redshift measurements and ~ 300 are galaxies at $z < 0.05$ (the low-redshift ratio is $\sim 13\%$, compared with 2% expected for a magnitude-limited survey).

S^5 is an on-going survey. We have observed ~ 25 nights in 2018 and 12 hrs in 2019 so far. More observations will be conducted in 2019. In addition to completing observations of the DES streams, we will also observe other streams in the Southern Hemisphere and Northern Hemisphere streams that are accessible from the Siding Spring Observatory.

Several papers presenting the spectroscopic results on the stellar streams are in preparation, with additional papers on other auxiliary science topics, ranging from the discovery of a hyper velocity star to studies of the low-redshift galaxies.

This paper is based on the S^5 internal data release version 1.4. The first public data release of S^5 , containing all observations taken in 2018 and 2019, is scheduled for the end of 2020. Updates on S^5 can be found at <http://s5collab.github.io>.

ACKNOWLEDGEMENTS

This paper includes data obtained with the Anglo-Australian Telescope in Australia. We acknowledge the traditional owners of the land on which the AAT stands, the Gamilaraay people, and pay our respects to elders past and present. This paper includes data gathered with the 6.5 meter Magellan Telescopes located at Las Campanas Observatory, Chile.

The S^5 Collaboration gratefully acknowledges a time swap with the Pristine Collaboration that enabled the 12 hours S^5 observation in 2019. We also would like to thank Anke Arentsen for helpful discussions on flux loss in the 2dF fibres (see Appendix A). Finally, we would like to thank Nicholas Martin for reviewing this paper.

TSL, APJ, and YYM are supported by NASA through Hubble Fellowship grant HST-HF2-51439.001, HST-HF2-51393.001, and HST-HF2-51441.001 respectively, awarded by the Space Telescope

Science Institute, which is operated by the Association of Universities for Research in Astronomy, Inc., for NASA, under contract NAS5-26555. SK is partially supported by NSF grant AST-1813881 and Heising-Simons foundation grant 2018-1030. J. D. Simpson, SLM and DBZ acknowledge the support of the Australian Research Council (ARC) through Discovery Project grant DP180101791. YYM was supported by the Pittsburgh Particle Physics, Astrophysics and Cosmology Center through the Samuel P. Langley PITT PACC Postdoctoral Fellowship. RHW, MG, and YYM received support from NSF AST-1517148. G. S. Da C. also acknowledges ARC support through Discovery Project grant DP150103294. J. D. Simon was supported in part by the National Science Foundation through grant AST-1714873.

This research has made use of the SIMBAD database, operated at CDS, Strasbourg, France (Wenger et al. 2000), and NASA’s Astrophysics Data System Bibliographic Services.

This work presents results from the European Space Agency (ESA) space mission Gaia. Gaia data are being processed by the Gaia Data Processing and Analysis Consortium (DPAC). Funding for the DPAC is provided by national institutions, in particular the institutions participating in the Gaia MultiLateral Agreement (MLA). The Gaia mission website is <https://www.cosmos.esa.int/gaia>. The Gaia archive website is <https://archives.esac.esa.int/gaia>.

This project used public archival data from the Dark Energy Survey (DES). Funding for the DES Projects has been provided by the U.S. Department of Energy, the U.S. National Science Foundation, the Ministry of Science and Education of Spain, the Science and Technology Facilities Council of the United Kingdom, the Higher Education Funding Council for England, the National Center for Supercomputing Applications at the University of Illinois at Urbana-Champaign, the Kavli Institute of Cosmological Physics at the University of Chicago, the Center for Cosmology and Astro-Particle Physics at the Ohio State University, the Mitchell Institute for Fundamental Physics and Astronomy at Texas A&M University, Financiadora de Estudos e Projetos, Fundação Carlos Chagas Filho de Amparo à Pesquisa do Estado do Rio de Janeiro, Conselho Na-

cional de Desenvolvimento Científico e Tecnológico and the Ministério da Ciência, Tecnologia e Inovação, the Deutsche Forschungsgemeinschaft, and the Collaborating Institutions in the Dark Energy Survey. The Collaborating Institutions are Argonne National Laboratory, the University of California at Santa Cruz, the University of Cambridge, Centro de Investigaciones Energéticas, Medioambientales y Tecnológicas-Madrid, the University of Chicago, University College London, the DES-Brazil Consortium, the University of Edinburgh, the Eidgenössische Technische Hochschule (ETH) Zürich, Fermi National Accelerator Laboratory, the University of Illinois at Urbana-Champaign, the Institut de Ciències de l'Espai (IEEC/CSIC), the Institut de Física d'Altes Energies, Lawrence Berkeley National Laboratory, the Ludwig-Maximilians Universität München and the associated Excellence Cluster Universe, the University of Michigan, the National Optical Astronomy Observatory, the University of Nottingham, The Ohio State University, the OzDES Membership Consortium, the University of Pennsylvania, the University of Portsmouth, SLAC National Accelerator Laboratory, Stanford University, the University of Sussex, and Texas A&M University. Based in part on observations at Cerro Tololo Inter-American Observatory, National Optical Astronomy Observatory, which is operated by the Association of Universities for Research in Astronomy (AURA) under a cooperative agreement with the National Science Foundation.

The Legacy Surveys consist of three individual and complementary projects: the Dark Energy Camera Legacy Survey (DECaLS; NOAO Proposal ID # 2014B-0404; PIs: David Schlegel and Arjun Dey), the Beijing-Arizona Sky Survey (BASS; NOAO Proposal ID # 2015A-0801; PIs: Zhou Xu and Xiaohui Fan), and the Mayall z-band Legacy Survey (MzLS; NOAO Proposal ID # 2016A-0453; PI: Arjun Dey). DECaLS, BASS and MzLS together include data obtained, respectively, at the Blanco telescope, Cerro Tololo Inter-American Observatory, National Optical Astronomy Observatory (NOAO); the Bok telescope, Steward Observatory, University of Arizona; and the Mayall telescope, Kitt Peak National Observatory, NOAO. The Legacy Surveys project is honored to be permitted to conduct astronomical research on Iolkam Du'ag (Kitt Peak), a mountain with particular significance to the Tohono O'odham Nation.

NOAO is operated by the Association of Universities for Research in Astronomy (AURA) under a cooperative agreement with the National Science Foundation.

The Legacy Survey team makes use of data products from the Near-Earth Object Wide-field Infrared Survey Explorer (NEOWISE), which is a project of the Jet Propulsion Laboratory/California Institute of Technology. NEOWISE is funded by the National Aeronautics and Space Administration.

The Legacy Surveys imaging of the DESI footprint is supported by the Director, Office of Science, Office of High Energy Physics of the U.S. Department of Energy under Contract No. DE-AC02-05CH1123, by the National Energy Research Scientific Computing Center, a DOE Office of Science User Facility under the same contract; and by the U.S. National Science Foundation, Division of Astronomical Sciences under Contract No. AST-0950945 to NOAO.

The national facility capability for SkyMapper has been funded through ARC LIEF grant LE130100104 from the Australian Research Council, awarded to the University of Sydney, the Australian National University, Swinburne University of Technology, the University of Queensland, the University of Western Australia, the University of Melbourne, Curtin University of Technology, Monash University and the Australian Astronomical Observatory. SkyMapper is owned and operated by The Australian National University's

Research School of Astronomy and Astrophysics. The survey data were processed and provided by the SkyMapper Team at ANU. The SkyMapper node of the All-Sky Virtual Observatory (ASVO) is hosted at the National Computational Infrastructure (NCI). Development and support the SkyMapper node of the ASVO has been funded in part by Astronomy Australia Limited (AAL) and the Australian Government through the Commonwealth's Education Investment Fund (EIF) and National Collaborative Research Infrastructure Strategy (NCRIS), particularly the National eResearch Collaboration Tools and Resources (NeCTAR) and the Australian National Data Service Projects (ANDS).

The Pan-STARRS1 Surveys (PS1) and the PS1 public science archive have been made possible through contributions by the Institute for Astronomy, the University of Hawaii, the Pan-STARRS Project Office, the Max-Planck Society and its participating institutes, the Max Planck Institute for Astronomy, Heidelberg and the Max Planck Institute for Extraterrestrial Physics, Garching, The Johns Hopkins University, Durham University, the University of Edinburgh, the Queen's University Belfast, the Harvard-Smithsonian Center for Astrophysics, the Las Cumbres Observatory Global Telescope Network Incorporated, the National Central University of Taiwan, the Space Telescope Science Institute, the National Aeronautics and Space Administration under Grant No. NNX08AR22G issued through the Planetary Science Division of the NASA Science Mission Directorate, the National Science Foundation Grant No. AST-1238877, the University of Maryland, Eotvos Lorand University (ELTE), the Los Alamos National Laboratory, and the Gordon and Betty Moore Foundation.

Funding for SDSS-III has been provided by the Alfred P. Sloan Foundation, the Participating Institutions, the National Science Foundation, and the U.S. Department of Energy Office of Science. The SDSS-III web site is <http://www.sdss3.org/>.

SDSS-III is managed by the Astrophysical Research Consortium for the Participating Institutions of the SDSS-III Collaboration including the University of Arizona, the Brazilian Participation Group, Brookhaven National Laboratory, Carnegie Mellon University, University of Florida, the French Participation Group, the German Participation Group, Harvard University, the Instituto de Astrofísica de Canarias, the Michigan State/Notre Dame/JINA Participation Group, Johns Hopkins University, Lawrence Berkeley National Laboratory, Max Planck Institute for Astrophysics, Max Planck Institute for Extraterrestrial Physics, New Mexico State University, New York University, Ohio State University, Pennsylvania State University, University of Portsmouth, Princeton University, the Spanish Participation Group, University of Tokyo, University of Utah, Vanderbilt University, University of Virginia, University of Washington, and Yale University.

This manuscript has been authored by Fermi Research Alliance, LLC under Contract No. DE-AC02-07CH11359 with the U.S. Department of Energy, Office of Science, Office of High Energy Physics. The United States Government retains and the publisher, by accepting the article for publication, acknowledges that the United States Government retains a non-exclusive, paid-up, irrevocable, world-wide license to publish or reproduce the published form of this manuscript, or allow others to do so, for United States Government purposes.

Facilities: Anglo-Australian Telescope (AAOmega+2dF); Magellan/Clay (MIKE)

Software: NUMPY (van der Walt et al. 2011), SCIPY (Jones et al. 2001), MATPLOTLIB (Hunter 2007), ASTROPY (Astropy Collaboration et al. 2013; Price-Whelan et al. 2018), EMCÉE (Foreman-Mackey et al. 2013), CARPY (Kelson 2003), MOOG (Snedden 1973; Sobek

et al. 2011), q3c (Koposov & Bartunov 2006), SKLEARN (Pedregosa et al. 2011), RVSPecFIT (Koposov 2019)

REFERENCES

- AAO Software Team 2015, 2dfdr: Data reduction software (ascl:1505.015)
- Abolfathi B., et al., 2018, *ApJS*, **235**, 42
- Allende Prieto C., et al., 2008, *AJ*, **136**, 2070
- Allende Prieto C., Koesterke L., Ludwig H. G., Freytag B., Caffau E., 2013, *A&A*, **550**, A103
- Alonso A., Arribas S., Martínez-Roger C., 1999, *A&AS*, **140**, 261
- Amidror I., 2002, *Journal of Electronic Imaging*, **11**, 157
- Astropy Collaboration et al., 2013, *A&A*, **558**, A33
- Balbinot E., et al., 2016, *ApJ*, **820**, 58
- Baldry I. K., et al., 2014, *MNRAS*, **441**, 2440
- Bechtol K., et al., 2015, *ApJ*, **807**, 50
- Belokurov V., Koposov S. E., 2016, *MNRAS*, **456**, 602
- Belokurov V., et al., 2007, *ApJ*, **654**, 897
- Belokurov V., Deason A. J., Erkal D., Koposov S. E., Carballo-Bello J. A., Smith M. C., Jethwa P., Navarrete C., 2019, *MNRAS*, **488**, L47
- Bernstein R., Shectman S. A., Gunnels S. M., Mochnacki S., Athey A. E., 2003, in Iye M., Moorwood A. F. M., eds, Society of Photo-Optical Instrumentation Engineers (SPIE) Conference Series Vol. 4841, Instrument Design and Performance for Optical/Infrared Ground-based Telescopes. pp 1694–1704, doi:10.1117/12.461502
- Bishop C. M., 2006, Pattern Recognition and Machine Learning (Information Science and Statistics). Springer-Verlag, Berlin, Heidelberg
- Bonaca A., Hogg D. W., 2018, *ApJ*, **867**, 101
- Bovy J., Bahmanyar A., Fritz T. K., Kallivayalil N., 2016, *ApJ*, **833**, 31
- Bovy J., Erkal D., Sanders J. L., 2017, *MNRAS*, **466**, 628
- Bowden A., Belokurov V., Evans N. W., 2015, *MNRAS*, **449**, 1391
- Breiman L., 2001, *Machine Learning*, **45**, 5
- Buder S., et al., 2018, *MNRAS*, **478**, 4513
- Bullock J. S., Johnston K. V., 2005, *ApJ*, **635**, 931
- Cannon R., Farrell T., Saunders W., Sharp R., Croom S., 2008, Anglo-Australian Observatory Epping Newsletter, **113**, 26
- Carlberg R. G., 2013, *ApJ*, **775**, 90
- Carrera R., Pancino E., Gallart C., del Pino A., 2013, *MNRAS*, **434**, 1681
- Casey A. R., 2014, PhD thesis, Australian National University
- Castelli F., Kurucz R. L., 2003, in Piskunov N., Weiss W. W., Gray D. F., eds, IAU Symposium Vol. 210, Modelling of Stellar Atmospheres. p. A20 (arXiv:astro-ph/0405087)
- Chambers K. C., et al., 2016, preprint, (arXiv:1612.05560)
- Clem J. L., 2006, PhD thesis, University of Victoria, Canada
- Clementini G., et al., 2019, *A&A*, **622**, A60
- Cui X.-Q., et al., 2012, *Research in Astronomy and Astrophysics*, **12**, 1197
- DES Collaboration et al., 2018, *ApJS*, **239**, 18
- DESI Collaboration et al., 2016, preprint, (arXiv:1611.00036)
- Dalton G., et al., 2012, in Ground-based and Airborne Instrumentation for Astronomy IV. p. 84460P, doi:10.1117/12.925950
- Deason A. J., Belokurov V., Evans N. W., 2011, *MNRAS*, **416**, 2903
- Deason A. J., Belokurov V., Evans N. W., An J., 2012, *MNRAS*, **424**, L44
- Deason A. J., Belokurov V., Koposov S. E., 2018, *ApJ*, **852**, 118
- Dey A., et al., 2019, *AJ*, **157**, 168
- Dotter A., Chaboyer B., Jevremović D., Kostov V., Baron E., Ferguson J. W., 2008, *ApJS*, **178**, 89
- Drlica-Wagner A., et al., 2015, *ApJ*, **813**, 109
- Erkal D., Belokurov V., 2015a, *MNRAS*, **450**, 1136
- Erkal D., Belokurov V., 2015b, *MNRAS*, **454**, 3542
- Erkal D., Sanders J. L., Belokurov V., 2016, *MNRAS*, **461**, 1590
- Erkal D., et al., 2019, *MNRAS*, **487**, 2685
- Foreman-Mackey D., Hogg D. W., Lang D., Goodman J., 2013, *PASP*, **125**, 306
- Frebel A., Casey A. R., Jacobson H. R., Yu Q., 2013, *ApJ*, **769**, 57
- Freeman K., Bland-Hawthorn J., 2002, *ARA&A*, **40**, 487
- Gaia Collaboration et al., 2018a, *A&A*, **616**, A1
- Gaia Collaboration et al., 2018b, *A&A*, **616**, A10
- Garavito-Camargo N., Besla G., Laporte C. F. P., Johnston K. V., Gómez F. A., Watkins L. L., 2019, preprint, (arXiv:1902.05089)
- Geha M., et al., 2017, *ApJ*, **847**, 4
- Gentile Fusillo N. P., et al., 2019, *MNRAS*, **482**, 4570
- Geweke J., 1992, in IN BAYESIAN STATISTICS. University Press, pp 169–193
- Gibbons S. L. J., Belokurov V., Evans N. W., 2014, *MNRAS*, **445**, 3788
- Gilmore G., et al., 2012, The Messenger, **147**, 25
- Goodman J., Weare J., 2010, Communications in Applied Mathematics and Computational Science, Vol.~5, No.~1, p.~65-80, 2010, **5**, 65
- Green A., Brough S., Zafar T., López-Sánchez A. R., Sharp R., Cannon R., Bridges T., 2017, Technical report, 2dF+AAOmega Manual, http://www.aao.gov.au/get/document/2dF-AAOmega-obs-manual.pdf. Australian Astronomical Observatory, Sydney, Australia, http://www.aao.gov.au/get/document/2dF-AAOmega-obs-manual.pdf
- Grillmair C. J., 2017, *ApJ*, **847**, 119
- Helmi A., Koppelman H. H., 2016, *ApJ*, **828**, L10
- Hinton S. R., Davis T. M., Lidman C., Glazebrook K., Lewis G. F., 2016, *Astronomy and Computing*, **15**, 61
- Holl B., et al., 2018, *A&A*, **618**, A30
- Hunter J. D., 2007, *Computing in Science & Engineering*, **9**, 90
- Husser T. O., Wende-von Berg S., Dreizler S., Homeier D., Reiners A., Barman T., Hauschildt P. H., 2013, *A&A*, **553**, A6
- Ibata R. A., Lewis G. F., 1998, *ApJ*, **500**, 575
- Ibata R., Lewis G. F., Irwin M., Totten E., Quinn T., 2001, *ApJ*, **551**, 294
- Ibata R. A., Lewis G. F., Irwin M. J., Quinn T., 2002, *MNRAS*, **332**, 915
- Ibata R. A., Lewis G. F., Martin N. F., 2016, *ApJ*, **819**, 1
- Ivezić Ž., et al., 2008, *ApJ*, **684**, 287
- Ji A. P., Simon J. D., Frebel A., Venn K. A., Hansen T. T., 2019, *ApJ*, **870**, 83
- Johnston K. V., Zhao H., Spergel D. N., Hernquist L., 1999, *ApJ*, **512**, L109
- Johnston K. V., Spergel D. N., Haydn C., 2002, *ApJ*, **570**, 656
- Jones E., Oliphant T., Peterson P., et al., 2001, SciPy: Open source scientific tools for Python, http://www.scipy.org/
- Kelson D. D., 2003, *PASP*, **115**, 688
- Kollmeier J. A., et al., 2017, preprint, (arXiv:1711.03234)
- Koposov S. E., 2019, RVSpecFit: Radial velocity and stellar atmospheric parameter fitting (ascl:1907.013)
- Koposov S., Bartunov O., 2006, in Gabriel C., Arviset C., Ponz D., Enrique S., eds, Astronomical Society of the Pacific Conference Series Vol. 351, Astronomical Data Analysis Software and Systems XV. p. 735
- Koposov S. E., Rix H.-W., Hogg D. W., 2010, *ApJ*, **712**, 260
- Koposov S. E., et al., 2011, *ApJ*, **736**, 146
- Koposov S. E., Irwin M., Belokurov V., Gonzalez-Solares E., Yoldas A. K., Lewis J., Metcalfe N., Shanks T., 2014, *MNRAS*, **442**, L85
- Koposov S. E., Belokurov V., Torrealba G., 2017, *MNRAS*, **470**, 2702
- Koposov S. E., et al., 2019a, preprint, (arXiv:1907.11725)
- Koposov S. E., et al., 2019b, *MNRAS*, **485**, 4726
- Lancaster L., Koposov S. E., Belokurov V., Evans N. W., Deason A. J., 2019, *MNRAS*, **486**, 378
- Lee Y. S., et al., 2008, *AJ*, **136**, 2022
- Lemon C. A., Auger M. W., McMahon R. G., Koposov S. E., 2017, *MNRAS*, **472**, 5023
- Lewis I. J., et al., 2002, *MNRAS*, **333**, 279
- Li T. S., et al., 2017, *ApJ*, **838**, 8
- Li T. S., et al., 2018a, *ApJ*, **857**, 145
- Li T. S., et al., 2018b, *ApJ*, **866**, 22
- Lindgren L., et al., 2016, *A&A*, **595**, A4
- Lindgren L., et al., 2018, *A&A*, **616**, A2
- Majewski S. R., et al., 2004, *AJ*, **128**, 245
- Majewski S. R., et al., 2017, *AJ*, **154**, 94
- Mateu C., Read J. I., Kawata D., 2018, *MNRAS*, **474**, 4112
- Miszalski B., Shortridge K., Saunders W., Parker Q. A., Croom S. M., 2006, *MNRAS*, **371**, 1537
- Morganson E., et al., 2018, *PASP*, **130**, 074501
- Narayan G., et al., 2019, *ApJS*, **241**, 20
- Pace A. B., Li T. S., 2019, *ApJ*, **875**, 77

- Pedregosa F., et al., 2011, *Journal of Machine Learning Research*, 12, 2825
- Price-Whelan A. M., et al., 2018, *AJ*, 156, 123
- Prusti T., et al., 2016, *A&A*, 595, A1
- Sandage A., 1969, *ApJ*, 158, 1115
- Sanders J. L., Bovy J., Erkal D., 2016, *MNRAS*, 457, 3817
- Schlafly E. F., Meisner A. M., Green G. M., 2019, *ApJS*, 240, 30
- Schlegel D. J., Finkbeiner D. P., Davis M., 1998, *ApJ*, 500, 525
- Schörck T., et al., 2009, *A&A*, 507, 817
- Sesar B., et al., 2015, *ApJ*, 809, 59
- Sharp R., et al., 2006, in *Society of Photo-Optical Instrumentation Engineers (SPIE) Conference Series*. p. 62690G ([arXiv:astro-ph/0606137](https://arxiv.org/abs/astro-ph/0606137)), [doi:10.1117/12.671022](https://doi.org/10.1117/12.671022)
- Sharp R., Brough S., Cannon R. D., 2013, *MNRAS*, 428, 447
- Shipp N., et al., 2018, *ApJ*, 862, 114
- Simpson J. D., et al., 2016, *MNRAS*, 459, 1069
- Snedden C. A., 1973, PhD thesis, THE UNIVERSITY OF TEXAS AT AUSTIN.
- Sobeck J. S., et al., 2011, *AJ*, 141, 175
- Varghese A., Ibata R., Lewis G. F., 2011, *MNRAS*, 417, 198
- Vickers J. J., Grebel E. K., Huxor A. P., 2012, *AJ*, 143, 86
- Wenger M., et al., 2000, *A&AS*, 143, 9
- Willey R. L., Burbidge E. M., Sandage A. R., Burbidge G. R., 1962, *ApJ*, 135, 94
- Wolf C., et al., 2018, *Publ. Astron. Soc. Australia*, 35, e010
- Wright E. L., et al., 2010, *AJ*, 140, 1868
- Yanny B., et al., 2000, *ApJ*, 540, 825
- Yong D., et al., 2013, *ApJ*, 762, 27
- Yoon J. H., Johnston K. V., Hogg D. W., 2011, *ApJ*, 731, 58
- York D. G., et al., 2000, *AJ*, 120, 1579
- Yuan F., et al., 2015, *MNRAS*, 452, 3047
- Zwitter T., et al., 2018, *MNRAS*, 481, 645
- de Jong R. S., et al., 2012, in *Ground-based and Airborne Instrumentation for Astronomy IV*. p. 84460T ([arXiv:1206.6885](https://arxiv.org/abs/1206.6885)), [doi:10.1117/12.926239](https://doi.org/10.1117/12.926239)
- van der Walt S., Colbert S. C., Varoquaux G., 2011, *Computing in Science & Engineering*, 13, 22
- New Jersey, Piscataway, NJ 08854, USA
- ¹⁵ Department of Physics and Astronomy, University of Pittsburgh, Pittsburgh, PA 15260, USA
- ¹⁶ Pittsburgh Particle Physics, Astrophysics, and Cosmology Center (PITT PACC), University of Pittsburgh, Pittsburgh, PA 15260, USA
- ¹⁷ Department of Astronomy, Yale University, New Haven, CT 06520, USA
- ¹⁸ George P. and Cynthia Woods Mitchell Institute for Fundamental Physics and Astronomy, and Department of Physics and Astronomy, Texas A&M University, College Station, TX 77843, USA
- ¹⁹ Research School of Astronomy and Astrophysics, Australian National University, Canberra, ACT 2611, Australia
- ²⁰ Department of Physics, University of Surrey, Guildford GU2 7XH, UK
- ²¹ Centre for Astrophysics and Supercomputing, Swinburne University of Technology PO box 218 Hawthorn Vic 3122 Australia
- ²² Centre of Excellence for All-Sky Astrophysics in Three Dimensions (ASTRO 3D), Australia
- ²³ Department of Physics, University of Wisconsin-Madison, 1150 University Avenue Madison, WI 53706, USA
- ²⁴ Kapteyn Instituut, Rijksuniversiteit Groningen, the Netherlands
- ²⁵ School of Physics and Astronomy, Monash University, Wellington Rd, Clayton 3800, Victoria, Australia
- ²⁶ Cerro Tololo Inter-American Observatory, National Optical Astronomy Observatory, Casilla 603, La Serena, Chile
- ²⁷ Department of Physics, Stanford University, 382 Via Pueblo Mall, Stanford, CA 94305, USA
- ²⁸ Kavli Institute for Particle Astrophysics & Cosmology, P.O. Box 2450, Stanford University, Stanford, CA 94305, USA
- ²⁹ SLAC National Accelerator Laboratory, Menlo Park, CA 94025, USA

AFFILIATIONS

- ¹ Observatories of the Carnegie Institution for Science, 813 Santa Barbara St., Pasadena, CA 91101, USA
- ² Department of Astrophysical Sciences, Princeton University, Princeton, NJ 08544, USA
- ³ Fermi National Accelerator Laboratory, P.O. Box 500, Batavia, IL 60510, USA
- ⁴ Kavli Institute for Cosmological Physics, University of Chicago, Chicago, IL 60637, USA
- ⁵ McWilliams Center for Cosmology, Carnegie Mellon University, 5000 Forbes Ave, Pittsburgh, PA 15213, USA
- ⁶ Institute of Astronomy, University of Cambridge, Madingley Road, Cambridge CB3 0HA, UK
- ⁷ Department of Physics & Astronomy, Macquarie University, Sydney, NSW 2109, Australia
- ⁸ Macquarie University Research Centre for Astronomy, Astrophysics & Astrophotonics, Sydney, NSW 2109, Australia
- ⁹ Sydney Institute for Astronomy, School of Physics, A28, The University of Sydney, NSW 2006, Australia
- ¹⁰ Lowell Observatory, 1400 W Mars Hill Rd, Flagstaff, AZ 86001, USA
- ¹¹ Australian Astronomical Optics, Faculty of Science and Engineering, Macquarie University, Macquarie Park, NSW 2113, Australia
- ¹² School of Physics, UNSW, Sydney, NSW 2052, Australia
- ¹³ Department of Astronomy & Astrophysics, University of Chicago, 5640 S Ellis Avenue, Chicago, IL 60637, USA
- ¹⁴ Department of Physics and Astronomy, Rutgers, The State University of

APPENDIX A: FIBRE POSITIONING ACCURACY

The Two-degree Field (2dF) fibre positioner has been a workhorse instrument of the Anglo-Australian Telescope (AAT) for over 20 years. In its current iteration, a robotic X-Y gantry picks and places magnetic buttons onto the metal field plate, with these buttons attached to about 40 metres of optical fibres. These fibres transmit the light from the focal plane of the telescope to either the AAOmega or HERMES spectrographs.

As with any fibre system, there are fibre-to-fibre throughput variations with 2dF (Sharp et al. 2013; Simpson et al. 2016). As discussed in Sharp et al. (2013) light loss can occur at many places along the light path: at the primary mirror, at the air-fibre interface, and within the fibre itself. Simpson et al. (2016) found that HERMES appeared to have fibre-to-fibre throughput variations at the fibre-spectrograph interface.

An additional source of lower-than-expected throughput is the fibre placement accuracy. If the fibre is placed in the focal plane off the position of the target, then less flux will be received at the spectrograph. The fibres observe about 2 arcsec of the sky (similar to the typical seeing at the AAT) and 2dF has a stated ability to place fibres to with an accuracy of 0.3 arcsec on the sky (Green et al. 2017). However, the transformation from celestial coordinates to X-Y Cartesian positions for the robot gantry is complicated and requires careful calibration (Cannon et al. 2008).

We found that in some of our fields that regions of the plate appeared to have lower than expected signal. Here we compare the median flux of a given spectrum to the *Gaia* *G* magnitude of the star. We limit this comparison to only the expected stream candidate stars. This is because we wish to exclude the blue stars (which would have a different spectral energy distribution (SED) in the infrared than red stars), and galaxies (for which the magnitudes were taken from a different photometric system; and they are also not our main targets of interest). For a given star, the median flux in the reduced spectrum was converted to a magnitude²¹ and subtracted from the *Gaia* magnitude of the star. A zero-point correction was applied equal to the median of all the magnitude difference in a given field. This analysis assumes that the SEDs of all our stars are similar enough that their flux in the near-IR can be compared to their *G* magnitude. Some of the fibre-to-fibre scatter will likely be caused by the colour distribution of the stars.

In the left column of Figure A1 we show the results for the Jhelum 10 field. This can be considered a well-behaved field. The median flux follow the trend with stellar magnitude, and there are no obvious effects on throughput with fibre number. There is a slight decrease in throughput at larger radius on the plate, but this is to be expected as the plate scale decreases at the edge. In the bottom panel we show the X-Y position on the plate of the star with a dot, and then a blue line up or a red line down to indicate if the star had more or less flux than expected. The length of this line is scaled to how large the magnitude offset was. There is a small amount of clumpiness of the distributions of stars with higher or lower than expected flux in the X-Y plane.

In the right column of Figure A1 is a badly behaved field, Jhelum 8. Some of the stars have much lower flux than would be expected for their magnitude. These are concentrated with fibre numbers around 75–125 and are located at the edge of the plate. In the bottom panel of the column, these stars are all located in the left-hand edge of the plate. Because of the highly spatial nature of this

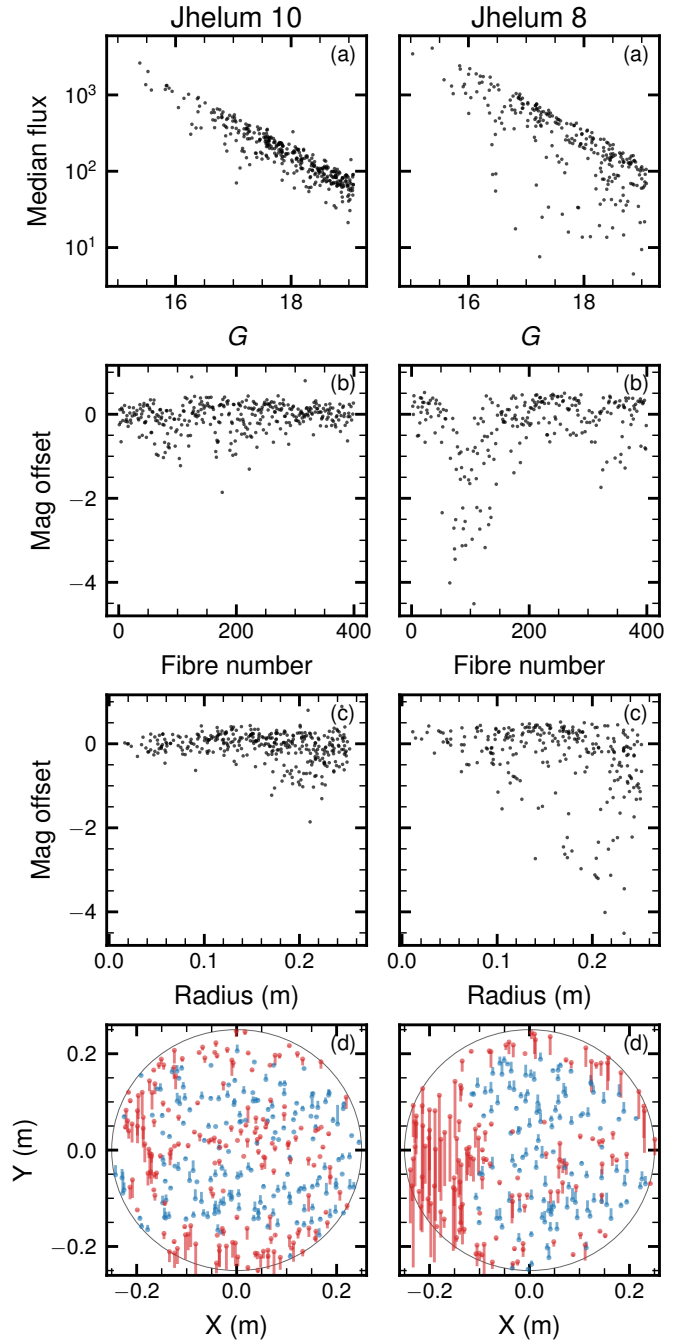


Figure A1. Comparison of the median spectral flux of the stream targets in Jhelum 10 (left column) and Jhelum 8 (right column) to their *Gaia* *G* magnitude. In (a) we show the trend of magnitude with median flux, where for Jhelum 8 a number of stars have much lower flux than would be expected. (b) and (c) gives the difference in magnitudes between the *G* magnitude and the median flux converted to a magnitude with respect to their fibre number and radius on the plate respectively. Stars above zero have more signal than expected, stars below have less signal than expected. In (d) we show the X-Y position on the plate with a dot, and then a blue line up or a red line down to indicate if the star had more or less flux than expected. For Jhelum 10, there is little structure of trends with position on the plate or fibre used. But for Jhelum 8, there is a clear region of the plate with apparently poor positioning.

²¹ We used $-2.5 \log(F)$, which does exclude stars with negative flux.

Table B1. A list of 674 QSOs identified by S^5 with robust redshift measurements. Columns from left to right are *Gaia* DR2 Source ID, RA, Declination, *G*-band magnitude, and measured redshift. The full table is available in the online version in machine readable format.

<i>Gaia</i> DR2 Source ID	RA (deg)	Decl. (deg)	<i>G</i> (mag)	redshift
4972649539728306432	4.697280	-51.759919	18.5	0.44
2362400547317486720	9.358120	-20.343325	19.1	1.85
2350270460161251200	9.375939	-21.322281	19.8	2.48
2350251115628542464	9.435354	-21.525050	19.9	1.82
2362705077678071424	9.917326	-20.550277	20.0	2.57
5001051196383860352	10.270612	-37.155282	19.6	0.72
5000985083952286336	10.317996	-37.613705	19.1	0.88
5001096894835994880	10.349795	-36.705281	19.4	2.24
2349979811134793088	10.383027	-21.975567	18.6	2.72
2349914531927728640	10.478138	-22.344380	19.5	3.31
2350032690772566016	10.534402	-21.499210	19.4	2.72
2350006886608763008	10.559899	-21.784944	18.9	2.22
5001085414388903296	10.682683	-36.794719	18.0	2.71
2349905697178722176	10.846492	-22.349365	19.4	1.83
2349949578860919040	10.867119	-22.030514	19.9	2.28
5001008345495272448	10.942463	-37.263972	19.4	0.85
2349122295143983360	10.977585	-22.865027	19.0	0.95
2349133427699269888	11.004514	-22.688900	18.1	2.17
5000707388546774272	11.038949	-38.288535	19.4	0.71
5001186436314116480	11.100714	-36.541186	19.5	1.91
5000764631871010432	11.106386	-37.986873	19.9	1.87
5000709381411691648	11.132341	-38.212503	18.7	0.73
5001112696020754304	11.157436	-36.966320	19.3	0.84
5001135102865013248	11.253751	-36.647412	19.8	0.76
...

on the plate, it is very likely to be an issue with the fibre placement, rather than other causes of fibre-to-fibre throughput variation.

We highlight this issue as it could potentially cause incompleteness in detecting the stream members. We emphasize that the *G*-band magnitude at $S/N = 5$ listed in Table 2 is the average magnitude over one AAT field. Due to the problem described above, we expect some fields have a number of stars brighter than the listed magnitude but with low S/N . As such we caution against drawing any assumptions related to the spatial clumpiness or gaps of our streams in terms of our detected members.

APPENDIX B: B. QSO REDSHIFTS

Over 1000 QSOs were identified spectroscopically via visual inspection. As QSO detection is not one of the main science goals of S^5 , we list in Table B1 674 QSOs that have secure redshifts. We note that an additional 412 QSOs were spectroscopically identified, but the limited spectral coverage of S^5 included only a single broad emission line, and therefore the redshifts could not be unambiguously determined. The spectra of all QSOs are available upon request.

APPENDIX C: THE VALIDATION OF 580V RADIAL VELOCITIES

The validation of the measurements from the blue arm (580V grating) requires first identifying spectra that are strongly affected by the bright moon and sky subtraction issues, leading to the contamination of the spectra by the Solar spectrum (see Section 3.2). The issues are particularly prominent in spectra of faint stars. To automatically identify these objects we train a random forest classifier to identify spectra with a large difference between 1700D RVs and 580 RVs, $|v_{580V} - v_{1700D}| > \sqrt{\sigma_{580V}^2 + \sigma_{1700D}^2}$ (indicative of

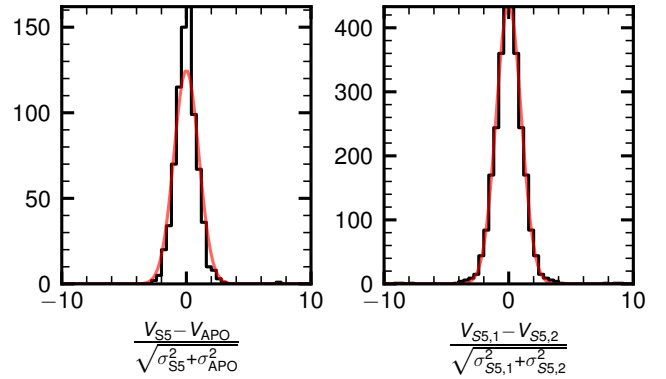


Figure C1. Comparison of S^5 radial velocities determined from blue arm (580V) spectra with APOGEE (left panel) and repeated S^5 observations (right panel). The Figure is identical to Figure 6 but is using radial velocities determined from the blue arm spectra.

580V sky subtraction issues), using the moon distance to the field, moon altitude above the horizon and moon phase as features. We train separate classifiers for stars with different *Gaia* magnitudes: $G < 15$, $15 < G < 16$, $16 < G < 17$, $17 < G < 18$, $18 < G < 19$ and $G > 19$. We set the `bad_moon` flag for stars identified by the classifier. In total $\sim 10,000$ stars are flagged. As expected, none of the bright stars are flagged, while for fainter stars the classifier mostly marks exposures where the moon phase is high and the moon is above the horizon.

To validate the RVs coming from the 580V spectra we follow the same steps as described in Section 4.1. We only use stars that are not affected by the Moon (i.e., those do not have the `bad_moon` flag set). This allows us to compute the offset of the velocities as well as calibrate the error model. Due to the much lower spectral resolution of the 580V grating compared to 1700D, as well as the lack of sky-lines for the wavelength calibration of science exposures, the offsets and systematic uncertainties of the 580V RVs are noticeably larger. We provide them here. The offset is $\sim 9 \text{ km s}^{-1}$.

$$v_{S5,580V} = v_{rvs,specfit} - 8.96 \text{ km s}^{-1}$$

The RV errors in the blue have a systematic floor of 21.06 km s^{-1} and the multiplicative factor of $k = 1.52$. Thus our final RV uncertainties in 580V are determined as

$$\sigma_{v,S5,580V} = \sqrt{(1.52 \sigma_{v,rvs,specfit})^2 + 21.06^2}$$

Figure C1 shows the validation of the re-calibrated 580V RVs and uncertainties using APOGEE data and repeated observations (similar to Figure 6).

This paper has been typeset from a $\text{\TeX}/\text{\LaTeX}$ file prepared by the author.